



Supplementary Materials for

N-Aryl Linked Spirocyclic Polymers For Membrane Separations of Complex Hydrocarbon Mixtures

Kirstie A. Thompson,[†] Ronita Mathias,[†] Daeok Kim, Jihoon Kim, Neel Rangnekar, J.R. Johnson, Scott J. Hoy, Irene Bechis, Andrew Tarzia, Kim E. Jelfs, Benjamin A. McCool, Andrew G. Livingston, Ryan P. Lively,* M.G. Finn*

*Correspondence to: ryan.lively@chbe.gatech.edu; mgfinn@gatech.edu

This PDF file includes:

Materials and Methods
Figs. S1 to S28
Tables S1 to S7
Spectral Data

Materials and Methods

Materials

Commercially-available diamines [*o*-tolidine (95%) and 1,5-diaminonaphthalene (97%) from Acros Organics; *m*-tolidine (>98%) and 2,5-dimethyl-1,4-phenylenediamine (>98%) from TCI] were rigorously purified before polymerization, as follows. The amine was suspended in H₂O followed by acidification with concentrated HCl. Additional H₂O was added until all amine was dissolved. The acidic diamine solution was then extracted with diethyl ether three times. The aqueous solution was boiled for 30 min while stirring in the presence of decolorizing charcoal (5-10 g, Acros Organics). The solution was allowed to cool to room temperature and the charcoal was removed by vacuum filtration. To the acidic aqueous solution was slowly added 1M NaOH with gentle stirring until the diamine precipitated. The diamine was then separated by vacuum filtration, washed with excess water and dried under vacuum overnight before use.

XantPhos (98%) was purchased from Acros Organics and STREM Chemicals. 1,4-dioxane (99.8% purity, anhydrous) was purchased from Sigma Aldrich in Sure/Seal™ bottles. Torlon® 4000T-LV powder was obtained from Solvay. Puramem® 280 membranes (Evonik High Performance Polymers) were purchased from Sterlitech Corporation. **PIM-1**, XantPhos Pd G3 precatalyst, XantPhos Pd G4 precatalyst, and IPr[HCl] were synthesized according to literature procedures (4, 12, 23, 24). All other chemicals were purchased from Sigma Aldrich, Acros Organics, Alfa Aesar, Oakwood Chemical, or TCI and used as received.

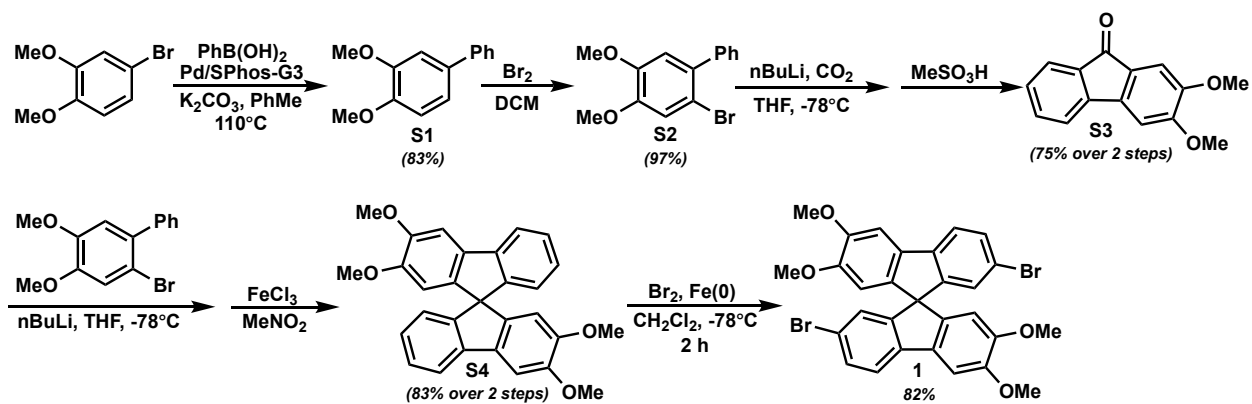
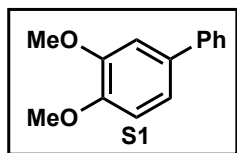


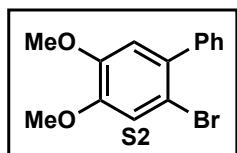
Fig. S1. Synthetic pathway toward 7,7'-dibromo-2,2',3,3'-tetramethoxy-9,9'-spirobifluorene (**1**).

Monomer Synthesis



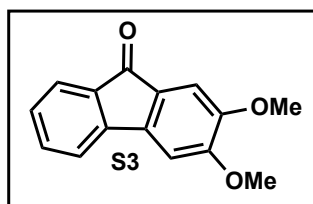
3,4-dimethoxy-1,1'-biphenyl: A 500 mL round-bottom flask equipped with a septum and magnetic stir bar was charged with 4-bromoveratrole (21.7 g, 100 mmol, 1.0 equiv), phenylboronic acid (14.5 g, 120 mmol, 1.2 equiv), potassium carbonate (34.5 g, 250 mmol, 2.5 equiv), and toluene (150 mL).

The capped flask was sparged with nitrogen for 15 min. Under nitrogen, the precatalyst SPhos-Pd-G4 (39.7 mg, 0.05 mmol, 0.05 mol %) was added in one portion. The flask was then capped and stirred at 110 °C overnight. The reaction mixture was cooled to room temperature, diluted with CH₂Cl₂, and filtered through a plug of Celite on top of silica gel. The resulting solution was concentrated by rotary evaporation and further dried under vacuum to provide the compound as an eggshell white solid (17.9 g, 83% yield). ¹H NMR (400 MHz, CDCl₃) δ 7.63 – 7.55 (m, 2H), 7.45 (dd, *J* = 8.4, 6.9 Hz, 2H), 7.38 – 7.31 (m, 1H), 7.21 – 7.12 (m, 2H), 6.98 (d, *J* = 8.2 Hz, 1H), 3.98 (s, 3H), 3.96 (s, 3H). ¹³C NMR (126 MHz, CDCl₃) δ 149.07, 148.54, 141.00, 134.20, 128.68, 126.82, 126.80, 119.34, 111.39, 110.39, 55.94, 55.89.



2-bromo-4,5-dimethoxy-1,1'-biphenyl: A 250 mL round-bottom flask equipped with a septum and magnetic stir bar was charged with 3,4-dimethoxy-1,1'-biphenyl (15 g, 70 mmol, 1 equiv) followed by the addition of CH₂Cl₂ (100 mL). With vigorous stirring, bromine (3.95 mL, 77 mmol, 1.1 equiv) was added dropwise followed by stirring at room temperature for

1 h. The reaction mixture was quenched with saturated aqueous sodium bicarbonate (~100 mL) followed by saturated sodium sulfite (~50 mL). The layers were separated, and the organic fraction was washed with water (1 x 50 mL) followed by brine (1 x 50 mL). The organic layer was then dried over anhydrous magnesium sulfate, filtered through a plug of silica gel, and concentrated by rotary evaporation. The crude product was triturated with methanol, filtered, and dried under vacuum to provide the title white solid (23.8 g, 97% yield). ¹H NMR (400 MHz, CDCl₃) δ 7.43 (tdd, *J* = 8.6, 6.0, 2.3 Hz, 5H), 7.15 (s, 1H), 6.86 (s, 1H), 3.94 (s, 3H), 3.89 (s, 3H). ¹³C NMR (126 MHz, CDCl₃) δ 148.68, 148.20, 141.06, 134.72, 129.48, 127.95, 127.38, 115.67, 113.80, 112.41, 56.20, 56.04.

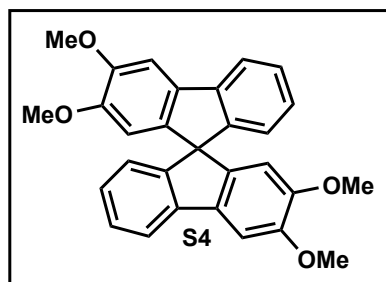


2,3-dimethoxy-9H-fluoren-9-one: A flame dried 1 L round-bottom flask equipped with a magnetic stir bar and rubber septum was charged with 2-bromo-4,5-dimethoxy-1,1'-biphenyl (22 g, 75 mmol, 1 equiv). The flask was evacuated and backfilled with argon three times. Dry tetrahydrofuran (375 mL) was added and the mixture was cooled to -78 °C under argon. A solution of *n*BuLi in hexanes (30 mL, 75 mmol, 1

equiv) was added dropwise. After addition, the mixture was stirred for 2 h at -78 °C. Carbon dioxide, produced from dry ice, was then bubbled through the reaction mixture until the deep yellow color of the reaction mixture dissipated to a pale yellow. The reaction mixture was allowed to warm to room temperature with a thin gauge needle inserted in the septum to prevent the buildup of pressure. The solvent was removed by rotary evaporation until a solid was obtained. The solid was then dissolved in water and washed with diethyl ether. The aqueous layer was acidified with aqueous HCl and the resulting yellow solid was filtered and dried under vacuum.

The intermediate was stirred in mixture of methanesulfonic acid (100 mL) and sulfuric acid (25 mL) at room temperature overnight. The resulting emerald green solution was then poured over ice (approximately 1L) resulting in the precipitation of a vibrant orange solid. The solid was

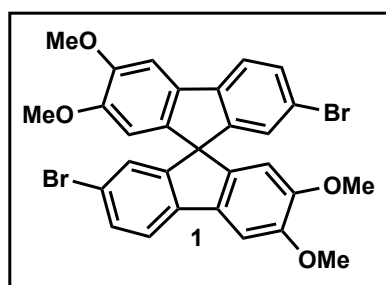
isolated by vacuum filtration, washed with excess water, recrystallized from methanol, and dried under vacuum to provide the title compound as a vivid orange solid (12.6 g, 70% yield). ^1H NMR (500 MHz, CDCl_3) δ 7.56 (dt, $J = 7.2, 0.9$ Hz, 1H), 7.42 (td, $J = 7.4, 1.2$ Hz, 1H), 7.37 (dt, $J = 7.3, 0.9$ Hz, 1H), 7.24 – 7.18 (m, 2H), 7.01 (s, 1H), 4.03 (s, 3H), 3.94 (s, 3H). ^{13}C NMR (126 MHz, CDCl_3) δ 193.16, 154.52, 149.67, 143.90, 139.44, 134.70, 134.19, 128.15, 126.80, 123.72, 119.06, 107.07, 103.36, 56.32, 56.21.



2,2',3,3'-tetramethoxy-9,9'-spirobifluorene: A flame-dried 500 mL round-bottom flask equipped with a stir bar and rubber septum was charged with 2-bromo-4,5-dimethoxy-1,1'-biphenyl (12.0 g, 41 mmol, 1 equiv). The flask was then evacuated and backfilled with argon three times. Dry tetrahydrofuran (275 mL) was added and the mixture was cooled to -78 °C under argon. A solution of *n*BuLi in hexanes (18 mL, 45.1 mmol, 1.1 equiv) was added dropwise. The reaction was allowed to stir for 2 h after

which 2,3-dimethoxy-9H-fluoren-9-one (8.2 g, 34 mmol, 0.83 equiv) was added in one portion. The reaction mixture was allowed to warm to room temperature, stirring overnight. The mixture was quenched with a saturated aqueous ammonium chloride (25 mL) and the tetrahydrofuran was removed from the mixture by rotary evaporation. The aqueous layer was extracted with CH_2Cl_2 (3 x 50 mL) and the combined organic layers were washed with H_2O , dried over MgSO_4 , and the solvent removed by rotary evaporation. The resulting off white crude solid was triturated with MeOH and dried under vacuum.

This intermediate was transferred to a 250 mL round bottom flask equipped with a stir bar. A small spatula scoop of FeCl_3 was added, along with nitromethane (65 mL). The reaction was allowed to stir for 30 min after which the reaction largely solidified; the remaining solvent was removed by rotary evaporation. The resulting material was dried under vacuum followed by trituration with MeOH. The resulting off-white solid was dried under vacuum to provide the title compound (12.3 g, 83% yield). ^1H NMR (500 MHz, CDCl_3) δ 7.93 – 7.52 (m, 2H), 7.36 (s, 4H), 7.05 (s, 2H), 6.88 – 6.53 (m, 2H), 6.26 (s, 2H), 4.05 (s, 6H), 3.67 (s, 6H). ^{13}C NMR (126 MHz, CDCl_3) δ 149.44, 149.26, 149.08, 141.87, 140.75, 134.22, 127.47, 126.50, 123.59, 118.75, 106.73, 102.83, 65.73, 56.11, 55.98.



7,7'-dibromo-2,2',3,3'-tetramethoxy-9,9'-spirobifluorene: A 100 mL round-bottom flask equipped with a stir bar and rubber septum was charged with 2,2',3,3'-tetramethoxy-9,9'-spirobifluorene (3.7 g, 8.5 mmol, 1 equiv) and $\text{Fe}(0)$ (190 mg, 3.4 mmol, 0.4 equiv). The flask was evacuated and backfilled with argon three times. Dry CH_2Cl_2 (30 mL) was added and the reaction mixture was cooled to -78 °C under argon. Bromine (1.3 mL, 25.5 mmol, 3 equiv) was added dropwise and the reaction

mixture was allowed to stir for 2 h. The reaction mixture was then poured into excess saturated aqueous sodium sulfite solution while stirring. The solution was extracted with CH_2Cl_2 (3 x 50 mL) and the organic layer was washed with water (1 x 50 mL), brine (1 x 50 mL), dried over MgSO_4 , and the solvent was removed by rotary evaporation. The crude material was then purified by column chromatography with a gradual gradient of ethyl acetate and hexanes (10% to 80% EtOAc), providing the title compound as a white solid (4.1 g, 82% yield). ^1H NMR (500 MHz,

CDCl_3) δ 7.59 (d, $J = 8.1$ Hz, 2H), 7.49 (dd, $J = 8.0, 2.0$ Hz, 2H), 7.32 (s, 2H), 6.78 (d, $J = 1.8$ Hz, 2H), 6.22 (s, 2H), 4.04 (d, $J = 2.8$ Hz, 6H), 3.69 (s, 6H). ^{13}C NMR (126 MHz, CDCl_3) δ 150.27, 149.92, 149.65, 140.85, 139.72, 133.11, 130.89, 126.78, 120.24, 120.10, 106.61, 102.95, 65.36, 56.16, 56.02.

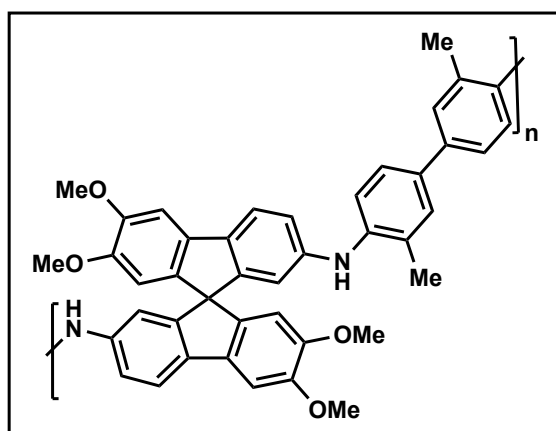
Polymer Synthesis

Limited reports have been made applying Buchwald-Hartwig as a polymerization method; some notable examples are listed (25-28).

For our purposes, bromination of the spirobifluorene monomer as above was followed by careful column chromatography to remove trace quantities of remaining starting material and a tribrominated byproduct. Similarly, rigorous purification of the commercially available diamines as described above was also found to be necessary, presumably due to the ready oxidation of these amines in air.

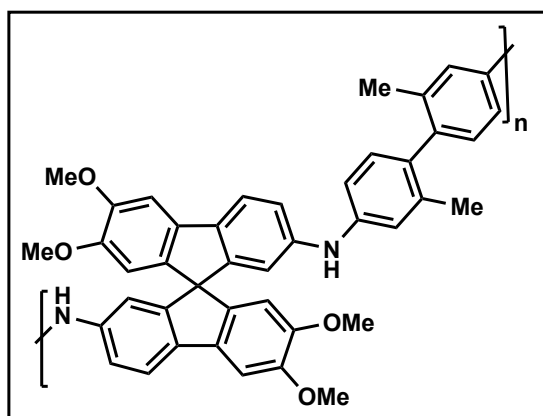
The Buchwald-Hartwig polymerization of **1** and *o*-tolidine (3,3'-dimethylbenzidine, compound **I** in Fig. 1) was explored with several known catalysts for this reaction, as summarized in Table S1. The palladacycle XantPhos Pd G4 (**12**) proved to be the most effective, giving the highest polymer molecular weight in good yield. (High molecular weights are desirable because longer chains form higher quality films, whereas short chains are more likely to cause cracking or to be too soluble in the organic mixtures to be separated.) Consistent with prior reports (**12**, **29**), polymerization catalyzed by the XantPhos Pd G3 pre-catalyst was much slower, requiring ten days to reach similar conversion and molecular weight (data not shown). $\text{Pd}(\text{dba})_2$ was also found to be inefficient in this process (Table S1, entries 4 and 5).

While polymerization reactions at 50 °C consistently produced soluble polymeric products, increasing the reaction temperature to 100 °C produced polymer gels that were largely insoluble. While this may be due to the intrinsic properties of larger chains, it is also possible that chain crosslinking occurred under these conditions, even a small amount of which can be expected to dramatically decrease solubility. Decreasing overall concentration at high reaction temperature (Table S1, reaction 2) eliminated the gelation problem, but also compromised chain length. To balance these effects, three of the four polymers were prepared at 80 °C. Unfortunately, the use of BrettPhos – known for its selective coupling of primary over secondary amines (**30**) – did not provide a significant degree of polymerization.



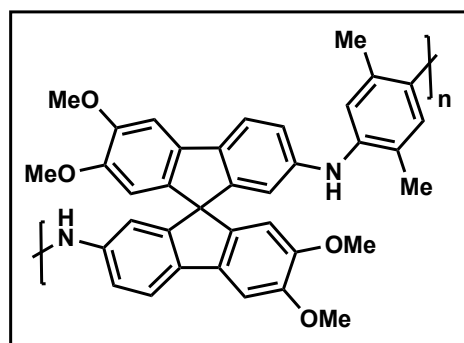
SBAD-1: A 10 mL microwave vial equipped with a stir bar and crimp cap was charged with *o*-tolidine (212.3 mg, 1 mmol, 1 equiv), 7,7'-dibromo-2,2',3,3'-tetramethoxy-9,9'-spirobifluorene (594.3 mg, 1 mmol, 1 equiv), sodium *tert*-butoxide (288.3 mg, 3 mmol, 3 equiv), and XantPhos-Pd-G4 (48.1mg, 0.05 mmol, 5 mol %). The tube was evacuated and backfilled with argon three times. Dry and air-free dioxane (5 mL, 0.2 M with respect to one monomer) was added and the reaction mixture was allowed to stir for 24 h at 50 °C in an oil bath. The resulting polymer appeared as a solid precipitate, which was isolated by filtration, dried, dissolved in the minimum volume of CHCl_3 , and precipitated by addition to methanol (500 mL). The solid was filtered, washed with excess

MeOH, and then refluxed in a solution of sodium diethyl dithiocarbamate (~30 mL, 0.25 M) overnight to remove any residual Pd. The polymer was filtered, rinsed with excess MeOH, and dried in a vacuum oven at 80 °C overnight to give a tan solid (521 mg, 81% yield). ¹H NMR (500 MHz, CDCl₃, 318 K) δ 7.56 (d, *J* = 8.1 Hz, 2H), 7.31 – 7.29 (m, 2H), 7.25 (s, 2H), 7.21 (d, *J* = 8.5 Hz, 2H), 7.10 (d, *J* = 8.3 Hz, 2H), 6.99 (dd, *J* = 8.6, 2.2 Hz, 2H), 6.37 (d, *J* = 2.1 Hz, 2H), 6.32 (s, 2H), 5.29 (s, 2H), 3.99 (s, 6H), 3.68 (d, *J* = 3.6 Hz, 6H), 2.17 (s, 6H); ¹³C NMR (126 MHz, CDCl₃) δ 151.16, 149.45, 148.72, 142.55, 140.45, 140.20, 134.82, 134.57, 133.98, 128.89, 127.49, 124.66, 119.36, 117.81, 116.96, 113.95, 107.42, 102.55, 65.62, 56.14, 43.95, 17.89. Analysis calculated for C₄₃H₃₆N₂O₄ C 80.10, H 5.63, N 4.34 Found C 78.10, H 5.77, N 4.24. GPC (against polystyrene standards, CHCl₃): M_n = 9.45 kDa, M_w = 80.4 kDa, D = 8.51.



SBAD-2: A 10 mL microwave vial equipped with a stir bar and crimp cap was charged with *m*-toluidine (159.2 mg, 0.75 mmol, 1 equiv), 7,7'-dibromo-2,2',3,3'-tetramethoxy-9,9'-spirobifluorene (445.7 mg, 0.75 mmol, 1 equiv), sodium *tert*-butoxide (216.2 mg, 2.25 mmol, 3 equiv), and XantPhos-Pd-G4 (36.1mg, 0.038 mmol, 5 mol %). The tube was evacuated and backfilled with argon three times. Dry and air-free dioxane (3.75 mL, 0.2 M with respect to one monomer) was added and the reaction mixture was allowed to stir for 24 h at 80 °C in an oil bath.

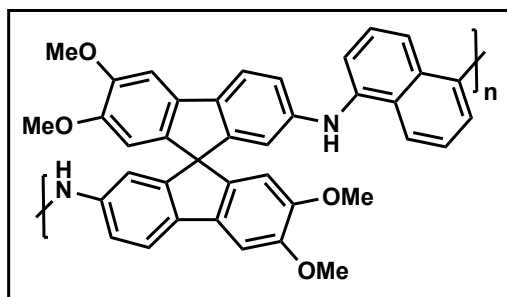
The polymer appeared as a solid precipitate, which was isolated by filtration, dried under vacuum, dissolved in the minimum volume of CHCl₃, and precipitated into methanol (500 mL). The solid was filtered, washed with excess MeOH, and refluxed in a solution of sodium diethyl dithiocarbamate (~30 mL, 0.25 M) overnight, filtered, and rinsed with excess MeOH. The resulting polymer was dried in a vacuum oven at 80 °C overnight providing a tan solid (280 g, 58% yield.) ¹H NMR (500 MHz, CDCl₃) δ 7.80 – 7.39 (m, 3H), 7.11 (s, 3H), 6.79 (d, *J* = 54.9 Hz, 6H), 6.36 (d, *J* = 38.0 Hz, 4H), 5.91 – 5.19 (m, 2H), 3.99 (d, *J* = 6.9 Hz, 6H), 3.84 – 3.41 (m, 6H), 1.88 (s, 6H). ¹³C NMR (126 MHz, CDCl₃) δ 151.16, 149.47, 148.79, 142.03, 141.96, 140.42, 140.41, 137.14, 134.97, 134.57, 133.87, 130.53, 119.32, 118.14, 117.08, 114.26, 107.42, 102.63, 65.59, 56.17, 56.10, 19.90. GPC (against polystyrene standards, CHCl₃): M_n = 10.3 kDa, M_w = 29.3 kDa, D = 2.85.



SBAD-3: A 10 mL microwave vial equipped with a stir bar and crimp cap was charged with 2,5-dimethyl-1,4-phenylenediamine (102.2 mg, 0.75 mmol, 1 equiv), 7,7'-dibromo-2,2',3,3'-tetramethoxy-9,9'-spirobifluorene (445.7 mg, 0.75 mmol, 1 equiv), sodium *tert*-butoxide (216.2 mg, 2.25 mmol, 3 equiv), and XantPhos-Pd-G4 (36.1mg, 0.038 mmol, 5 mol %). The tube was evacuated and backfilled with argon three times. Dry and air free dioxane (3.75 mL, 0.2 M with respect to one monomer) was added and the reaction mixture was allowed to stir for 24 h

at 80 °C in an oil bath. The polymer appeared as a solid precipitate, which was isolated by filtration, dried under vacuum, dissolved in the minimum volume of CHCl₃, and precipitated into methanol.

The solid was filtered, washed with excess MeOH, and refluxed in a solution of sodium diethyl dithiocarbamate (~30 mL, 0.25 M) overnight, filtered, and rinsed with excess MeOH (500 mL). The resulting polymer was dried in a vacuum oven at 80 °C overnight providing a tan solid (421 g, 98% yield). ¹H NMR (500 MHz, CDCl₃) δ 7.73 – 7.38 (m, 2H), 7.26 – 7.02 (m, 2H), 6.98 – 6.57 (m, 4H), 6.30 (dq, *J* = 23.5, 11.8 Hz, 4H), 5.38 – 4.79 (m, 2H), 4.12 – 3.73 (m, 6H), 3.67 (d, *J* = 21.3 Hz, 6H), 2.12 – 1.65 (m, 6H). ¹³C NMR (126 MHz, CHCl₃) Complex spectra due to polymer oxidation. Analysis calculated for C₃₇H₃₂N₂O₄ C 78.15, H 5.67 N 4.93 Found C 77.33 H 6.43 N 4.00. GPC (against polystyrene standards, CHCl₃): M_n = 10.3 kDa, M_w = 64.6 kDa, D = 6.25.



SBAD-4: A 10 mL microwave vial equipped with a stir bar and crimp cap was charged with 1,5-diaminonaphthalene (158 mg, 1 mmol, 1 equiv), 7,7'-dibromo-2,2',3,3'-tetramethoxy-9,9'-spirobifluorene (594 mg, 1 mmol, 1 equiv), sodium *tert*-butoxide (289 mg, 3 mmol, 3 equiv), and XantPhos-Pd-G4 (48.1mg, 0.05 mmol, 5 mol %). The tube was evacuated and backfilled with argon three times. Dry and air free dioxane (10 mL, 0.1 M with respect to one monomer)

was added and the reaction mixture was allowed to stir for 48 h at 80 °C in an oil bath. The polymer appeared as a solid precipitate, which was isolated by filtration, dried under vacuum, dissolved in the minimum volume of CHCl₃, and precipitated into methanol (500 mL). The solid was filtered, washed with excess MeOH, and refluxed in a solution of sodium diethyl dithiocarbamate (~10 mL, 0.25 M) overnight, filtered, and rinsed with excess MeOH. The resulting polymer was dried in a vacuum oven at 80 °C overnight providing a tan solid (373 g, 63% yield). ¹H NMR (500 MHz, CDCl₃) δ 7.81 – 7.35 (m, 4H), 7.28 – 6.66 (m, 8H), 6.64 – 6.05 (m, 4H), 5.82 (s, 2H), 4.19 – 3.77 (m, 6H), 3.77 – 3.35 (m, 6H). ¹³C NMR (126 MHz, CDCl₃) δ 151.17, 149.47, 148.79, 143.09, 140.46, 139.57, 135.02, 134.54, 133.80, 128.03, 125.42, 119.40, 117.16, 114.13, 107.44, 103.17, 103.00, 102.61, 65.63, 56.15, 56.12. GPC (against polystyrene standards, CHCl₃): M_n = 7.90 kDa, M_w = 57.0 kDa, D = 7.22.

Polymer characterization

Gel permeation chromatography (GPC, Fig. S3) was carried out using a TSKgel SuperH₂M-M (6.0 mm I.D. x 15 cm, 3.5 μm) column with a flow rate of 0.45 mL/min. Molecular weight was determined from a calibration of polystyrene standards. The number-average molecular weights of the polymers derived from the optimized procedures described above (calibrated against polystyrene, and so of uncertain absolute value) were all low, reflecting degrees of polymerization below 20, but dispersities were very large. This likely reflects two factors: (a) while the catalyzed Buchwald-Hartwig reaction is fast, the thermodynamic driving force of each coupling step is not large, and (b) branching via C-N bond formation to secondary amine centers is possible, and only a small amount of branching at secondary amine centers is necessary to dramatically inflate the observed weight-average molecular weight and dispersity. The polymerization results are highly reproducible, thus branching, if it occurs, is likely an intrinsic feature of the polymerization reaction.

Nuclear magnetic resonance (NMR) spectra were obtained on a Bruker AMX-400 and or Bruker DRX-500 instrument in CDCl₃ and referenced to the signals of residual protons in the NMR solvent.

Thermogravimetric analysis (TGA, Fig. S4) was used to evaluate the thermal stability of the polymers and determine the amount of non-solvent present in the powder after drying at 110 °C for 1 hour. The powders were heated to 900°C at 5°C/min under a nitrogen purge rate of 10 mL/min (TGA Q500, TA Instruments) and subsequently cooled at 10°C/min to room temperature.

Dynamic scanning calorimetry (DSC, Fig. S5) was performed by heating samples to 900 °C at a rate of 5 °C/min under 120 mL/min of N₂ (STA 449F3 F3 Jupiter, NETZSCH) to determine the glass transition and melting points of each polymer.

Sorption of N₂ (at 77 K) and CO₂ (at 273 K) were measured at relative pressures ranging from 1E-6 to 1 bar with an ASAP 2020 (Micromeritics) analyzer (Fig. 1B, Fig. S6A). The polymer powders were degassed for 12 h under vacuum at 110 °C immediately prior to analysis. CO₂ is a known plasticizer of **PIM-1** at higher activities with a kinetic diameter lower than N₂. As shown in Fig. 1B, the **SBAD** isotherms are more comparable to that of **PIM-1** in the case of CO₂ (although still lower) and have lower slopes at higher CO₂ activities.

The accessible free volume and swelling effect of CO₂ is quantified through the dual-mode sorption model shown in Equation 1. The CO₂ sorption isotherm can be fit to this model, which is characterized by the algebraic sum of Henry's law for a gas dissolving in a solid and a Langmuir equation for gas adsorbing in the free volume sites of the polymer network (31).

$$C = C_D + C_H = k_D p + \frac{C'_H b p}{1 + b p} \quad (1)$$

The Henry's law coefficient, k_D can be correlated to the sorption or swelling affinity of the polymer in a gas. The Langmuir capacity constant, C'_H , is related to the unrelaxed free volume of the glassy polymer. Fig. S6B and C shows the calculated k_D and C'_H values, respectively, obtained by best fit to the CO₂ sorption data compared to data obtained for a non-porous polymer such as Torlon[®] at the same temperature. Lower k_D values confirm that **SBAD** polymers undergo less CO₂-induced swelling than **PIM-1**, but are not as resistant as Torlon[®], which is extensively H-bonded throughout its network (32). The **SBAD** C'_H values were all somewhat lower than those for **PIM-1** (~4x difference) but significantly higher than those for Torlon[®] (>10x difference). These CO₂ vapor physisorption results suggest that the **SBAD** polymers possess higher cohesive energy densities than **PIM-1** and are thereby likely to be more resistant to solvent-induced swelling. This prediction was confirmed for thick films of **SBAD-1** submerged in toluene as discussed in the main text and shown in Fig. 1C.

The **SBAD-3** and **SBAD-4** polymers were much more colored (vibrant magenta and deep indigo, respectively) than the others in both the solid state and solution (Fig. S2). This may reflect their greater degrees of π -conjugation across the diamine linkage, allowing for small amounts of N-oxidation to lead to stronger donor-acceptor chromophores in the polymer backbone. The presence of such oxidized linkages may contribute to the more complex appearances of the NMR spectra and TGA analyses of these materials (Fig. S4).

Polymer model generation

The amorphous structural models for the PIMs were generated with the simulated polymerization algorithm Polymatic (15). Three independent models for each polymer were generated by randomly packing monomers in a periodic box of 70 Å with a one-to-one ratio at an initial low density of 0.3 - 0.4 g cm⁻³, as done in previous work (33). Previous work has also shown that three models are sufficient for sampling different structures and thus creating representative models that characterize the porosity of these systems, because the standard deviation between

models is small (33). For the construction of **PIM-1**, previously published procedures were used as reference (15). The structures were described using the polymer consistent force field (pcff) (34). Partial charges were calculated for the repeat units by fitting atomic charges from the output of Gaussian16 (35) calculations at the HF/6-31G* level of theory. The molecular models used to derive the charges include the repetition of each monomer twice, in order to derive charges for both the units inside the chain and at the end of the chain, saturated with capping functional groups. In the polymerization phase, bonds were formed between reactive atoms on different monomers within a cutoff of 6 Å. The reactive groups were the aromatic carbon connected to bromine in the spirobifluorene dibromide monomer and the nitrogen for the diamine monomers. The structure was minimized after every new bond was formed, while intermediate molecular dynamics (MD) steps in the canonical ensemble were performed once every five new bonds were formed, to allow the structure to adapt and the polymerization to continue, reaching high degrees of polymerization and therefore longer chains. The MD steps were performed at 1000 K for 10 ps using a timestep of 1 fs. Additional opposite fractional charges of 0.3 e were added to opposite reactive sites for all the PIMs to aid the polymerization.

Geometric restrictions for **PIM-1** were tested to obtain realistic structures, as described elsewhere (15), however, we found that these restrictions resulted in low degrees of polymerization of the structures compared to reported structures, whereas removing the restrictions resulted in similar degrees of polymerization to those previously reported (15). We carefully examined the models for any signs of incorrect bonding that the restrictions are supposed to avoid, but did not find any problems in the absence of the restrictions. All qualitative discussion of the differences between **PIM-1** and the other four models held regardless of whether we did or did not employ the restrictions. Bromine and hydrogen atoms were used to saturate unreacted active sites on the spirobifluorene and diamine monomers, respectively, after polymerization of **SBAD-1**, **SBAD-2**, **SBAD-3** and **SBAD-4**. Fluorine and hydrogen atoms were used to saturate the unreacted aromatic carbon and unreacted oxygen atoms in **PIM-1**, respectively. The monomers and the capping groups used for each system are reported in Fig. S7. Selected atom types and derived partial charges for all the atoms in the monomers are reported in Fig. S7 and Table S2.

The final polymerized structures were then annealed through a 21-step molecular dynamics equilibration, an established protocol for generating physically sensible structures of microporous polymers (15). A final temperature value (T_{Final}) of 300 K, a maximum temperature value (T_{Max}) of 1000 K, a final pressure value (P_{Final}) of 1 bar and a maximum pressure value (P_{Max}) of 5×10^5 bar were used for the annealing step. The LAMMPS package (36) was used to perform all the energy minimization and molecular dynamics across the structure generation procedure. Ewald summation was used to compute the long-range electrostatic interactions, the Lennard-Jones (LJ) potential was used to represent the short-range van der Waals interactions. The cut-off distance for the LJ interactions and the real part of the Ewald summation was set to 15 Å. Constant pressure and temperature were maintained using a Nosé-Hoover thermostat and barostat during molecular dynamics steps.

Polymer model analysis

The final structures obtained after annealing were used for the analysis. All the obtained results are averaged over the three different models for each structure. For the porosity analysis, Zeo++ (37, 38) was used, which uses a Voronoi decomposition to calculate void space, pore size distribution and the interconnectivity between voids given a certain probe radius. The structure is treated as rigid, therefore the flexibility of the system is not taken into account in the porosity

evaluation. The accessible and non-accessible surface area in the structures were calculated with a probe diameter of 2 Å, 2.2 Å, 3.30 Å (kinetic diameter of CO₂) and 3.64 Å (kinetic diameter of N₂)(39). The calculations were performed using the high accuracy flag. Surface areas were calculated using 5000 samples (number of MC samples per atom). Pore size distributions were calculated using 50000 samples per cell. For the pore size distribution shown in Fig. S16, 200000 samples were used. For the accessible and inaccessible surface area visualized in Figs. S9 and S10, 3000 – 4000 samples per atom were used.

Table S3 reports the values of the density of the initial random packing of monomers in the model box, together with the percentage of polymerization reached and the final value of bulk density after the annealing procedure. The standard deviations between different models for the same polymer are reported in parenthesis. **PIM-1** models reached the highest percentage of polymerization, which results in longer chains within the model, as can be seen from Fig. S8 which shows the chain length distribution inside the models. In Table S3, the diameters of the largest included sphere (D_I), largest free sphere (D_F) and largest included sphere along the free sphere path (D_{IF}) is reported for all the models. In particular, the D_F value defines the largest probe that can diffuse from one side to the other side of the model through interconnected pores. Given the D_F values in Table S3, none of the polymer models present accessible pores for a probe radius of 1.82 Å, corresponding to the kinetic diameter of N₂, contrary to experimental results. However, the analysis of the static model does not take into account the chain movement that can occur upon gas adsorption due to chain flexibility, and only a small amount of motion would conceivably be required for the **PIM-1** models ($D_F = 3.18$ (0.34)) to become interconnected to a nitrogen sized molecule.

PIM-1 has the highest value of total surface area (including both accessible and non-accessible voids) with respect to every tested probe diameter. This is reported visually in Fig. S9 and Fig. S10 for 2.2 Å and 3.64 Å probe diameters. Fig. S15 reports the pore size distribution inside all of the models, calculated using a probe diameter of 2 Å. **PIM-1** shows a wider distribution of pore sizes, up to 12 Å in diameter. The sampled pores and their location in each structure are reported in Fig. S16, where they are color-coded according to their size. The new class of **SBAD** polymers shows less interconnected porosity compared to **PIM-1**. This results from a more efficient packing of the polymer chains in the bulk structure, as shown by the average final densities for all the **SBAD** polymer models being higher than that obtained for the **PIM-1** models (Table S3). We analyzed whether the fact that the **SBAD** polymer chains have the potential to form hydrogen bonding also influences the more efficient packing and consequent lowering of porosity in the **SBAD** systems compared to **PIM-1**. However, analysis of the radial distribution function of hydrogen bond donor and acceptor atoms in the models did not show any evidence of this. The distribution of the values of two significant dihedral angles in all the models were plotted to confirm the higher flexibility in the new **SBAD** polymers compared to **PIM-1** (Fig. S13), the first including the spiro center, the second involving the linkage between the two monomers in the polymeric unit (as highlighted in Fig. S13). We find that the **PIM-1** distribution of the dihedral angle involving the spiro center is slightly narrower, which is an indication of the **PIM-1** chains having lower flexibility. In the case of the dihedral angle involving the linkage between the two monomers, the double linked nature of this linkage in **PIM-1** restricts the values of the angle around 180°, while in the case of the **SBAD** series there is an even distribution of the dihedral angle around 0° and 180°, coming from the different orientation that the diamine monomer can adopt with respect to the spirobifluorene monomer when the single amine linkage is formed. This helps enforce the more ladder-like chain morphology in the case of **PIM-1**.

The main differences between the structural arrangement of the **SBAD** chains compared to **PIM-1** are better highlighted by visual inspection. Fig. S12 shows the images of selected single chains for all the constructed models. We selected two chains for each polymer that are representative of the typical chain shape and arrangement in all the models for that system. However, it has to be kept in mind that every chain is different and unique in both its length and spatial arrangement. As can be seen from the stick representation of the chains (Fig. S12), **PIM-1** shows the expected ladder-like structure, while **SBAD** polymers seem to arrange themselves more in a spiral-like way. In general, **PIM-1** chains maintain a more linear arrangement, while the **SBAD** polymers tend to twist on themselves to form clusters. The **SBAD** polymers also have a higher degree of aromatic and conjugated systems, that can form inter- and intra-chain π - π interactions that can lead to a tighter packing. Fig. S14 shows examples of these chain-chain aromatic interactions.

Computational Polymer Swelling

Each annealed model of **PIM-1**, **SBAD-1** and **SBAD-3** was artificially swollen using the approach developed by Colina et al. (40). The swelling procedure generates models at different swelling percentages by expanding the systems' periodic box length (L) by a dilation factor, f . The annealed structure was considered a model with 0% swelling. The change in volume ($\Delta V/V$) due to swelling (or swelling percentage) is given by

$$\frac{\Delta V}{V} = \frac{(fL)^3}{L^3} - 1 \quad (2)$$

After expansion, the atom positions are remapped to equivalent relative positions in the new simulation box. Values of f in this work ranged from 1.000-1.225, and the corresponding $\Delta V/V$ values ranged from 0.00% to 83.83%. The swollen system was then equilibrated using two sequential MD simulations in the NVT (canonical) ensemble at 600 K for 100 ps and 300 K for 50 ps, respectively. An artificial swelling procedure was applied because simulating adsorption-based swelling was deemed computationally intractable. Crucially, the artificial swelling procedure does not include sorbates.

The role of swelling on the potential porosity of **PIM-1**, **SBAD-1** and **SBAD-3** was examined using the geometrical porosity calculated by Zeo++ (using the same sampling and probe sizes as the non-swollen models). Fig. S11 (a) and (b) show the effect of swelling on the average pore limiting diameter (D_F) of the models. In all cases, D_F increases as a function of swelling, but for **SBAD-1** and **SBAD-3**, D_F does not become larger than the diameter of CO_2 and N_2 until between 12-14% swelling. Therefore, in these models, **SBAD-1** and **SBAD-3** maintain non-interconnected voids (and low porosity) for low swelling values, unlike **PIM-1**. This result is further highlighted by the calculated accessible surface areas for probe sizes of CO_2 and N_2 in Fig. S11 (c) and (d), respectively. **PIM-1** shows accessible porosity to these probes at 3% swelling, while **SBAD-1** and **SBAD-3** have no accessible surface area until 12-14% swelling. It is important to note that the artificial swelling procedure does not entirely capture the physical process of swelling, i.e., swelling is not the only physical process causing the porosity of the PIMs in this study. Even though this approach is crude, these findings highlight preliminary indicators of the impact of polymer chemistry on the evolution of porosity due to dilations in PIM materials.

Membrane fabrication, characterization, and performance

A dense film of **SBAD-1** was prepared by pouring a 10 wt% chloroform solution of the polymer into a leveled Teflon dish in a glove bag saturated with chloroform vapor. The disk was allowed to stand for 24 h, and the film was then allowed to dry as the atmosphere was gradually depleted of solvent vapor over the course of 3 days. The film was then further dried under vacuum (-29 mm Hg) at 110 °C overnight. The degree of sorption in liquid hydrocarbon was measured by submerging weighed fragments of the films in toluene at room temperature (22 °C). The resulting solvated films were weighed after wiping the surface dry with a Kimwipe. Each measurement was performed twice using different fragments of film to improve accuracy. The solvent uptake at unit activity was calculated as

$$\text{Mass Change (\%)} = \frac{m_{\text{swollen}} - m_{\text{dry}}}{m_{\text{dry}}} \cdot 100 \quad (3)$$

Membrane supports were prepared using polyetherimide (PEI, ULTEM 1000) powder that was evacuated at 100 °C 12 h before use. A 23 wt% dope solution of PEI was prepared by dissolving the powder in a binary mixture of GBL/NMP (70/30 on a weight basis) by stirring at 70 °C for one day and then filtered using nylon net filter (11 µm pore size, Millipore) and stored for a day at room temperature to remove bubbles. Membranes were cast from the PEI dope solution on polyethylene terephthalate (PET) non-woven backing (Hirose) by using a continuous casting machine (SeptraTek, Korea) with a casting knife set at 170 µm. The casted film was plunged into a water bath set to 19°C to induce phase inversion. To enhance the chemical stability of PEI membranes for the usage in various organic solvents, PEI polymeric chains were crosslinked using diaminopropane (DAP) by immersing in a solution of 1 wt% of DAP in MeOH for 1 day, then placed in a solution of 5 wt% of DAP in MeOH for 22 h. At the end of the reaction, membranes were thoroughly rinsed with water and IPA and then dried at room temperature.

Thin film composites were produced from chloroform solutions of each polymer (**PIM-1**, 0.5 wt%) (**SBAD** series, 2 wt%), filtered through 0.2 µm PTFE syringe filters (VWR) and chilled to 4 °C overnight. Using a 25 µm stainless steel bar applicator (Gardco), each solution was blade-coated onto a flat crosslinked polyetherimide (PEI) prepared as described above. The nascent polymer film was allowed to dry overnight at room temperature in a fume hood before circular coupons with an effective surface area of 14 cm² were cut out for testing. Although the **PIM-1** solution was less concentrated, thicker films were observed compared to the SBAD series (Fig. S17) which could be due to lower polymer solution penetration through the support during casting as a result of its higher viscosity and lower polymer density.

Field Emission Scanning Electron Microscopy (FE-SEM) was used to obtain ultra-high-resolution images of the thin film composites (Hitachi SU8010). Samples were cut with a sharp razor blade and placed on aluminum mounts using carbon tape. A turbomolecular pumped coater (Quorum Q-150 T ES) was used to sputter coat the samples with a layer of a gold/palladium alloy under a deposition current of 10 mA for 45 seconds. Images were obtained with a voltage of 3kV and a current of 10 µA at a working distance of 8 mm (Fig. S17).

Permeation was measured with a custom-built cross flow system (Fig. S18) pressurized by an HPLC pump (Azura P 4.1S, Knauer). A binary mixture of 1 mol% triisopropylbenzene (TIPB) in toluene was used as a probe hydrocarbon separation feed. The mixture was pressurized to 15 bar at a feed flow rate of 10 mL/min. Aliquots from the permeate were taken at 24 h intervals until the permeance and rejection were stabilized for 24 h. The permeance (specifically, the

hydraulic permeance), $\frac{P}{\ell}$, is the total flux, J_i , of the permeating species through the membranes, normalized by the applied pressure, Δp .

$$\frac{P_i}{\ell} = \frac{J_i}{\Delta p} \quad (4)$$

The stage cut, defined as the ratio of permeate flow rate to feed flow rate, was maintained below 5% to reduce concentration polarization effects on the feed side of the membrane; concentration polarization can reduce the observed rejection of the solute. The rejection of TIPB solute was determined using gas chromatography (Agilent 7890B) and was calculated as the difference in concentration of the solute in the feed and permeate, normalized by the concentration in the feed.

$$\text{Rejection (\%)} = \frac{(C_{\text{feed}} - C_{\text{permeate}})}{C_{\text{feed}}} * 100 \quad (5)$$

Samples from each membrane sheet were tested in triplicate to assess the reproducibility of the separation performance (Fig. S19).

Standardized molecular weight cutoff performance was measured using 0.05 g•L⁻¹ of α -methylstyrene dimer (Sigma Aldrich, UK) and 0.5 g•L⁻¹ each of PS 580 and PS 1090 (Polymer Labs, UK), dissolved in toluene. Thin film composites of **SBAD-1** were tested in cross flow at 30 bar and those of **PIM-1** were tested at 5 bar (the maximum pressure these membranes could hold in the system due to high permeate flux) at a flow rate of 10 mL min⁻¹. The permeate was collected every 24 hours for at least 3 days until the rejection and permeance were steady (Fig. S20). The rejections of oligomers were analyzed by high-pressure liquid chromatography (Agilent HPLC) with a UV/Vis detector set at a wavelength of 264 nm. The MWCO was determined by interpolating the rejections of the marker solutes and is defined as the smallest molecular weight that corresponds to a 90% rejection.

Hydrocarbon molecular weight cut-off (Fig. S21) was determined by combining data from two separate mixtures: 1) A 7-component mixture containing 1 mol% each of the aromatic hydrocarbons listed as components 1-6 in Table S4 in toluene. The mixture was supplied through cross flow filtration at 20 mL/min at 10 bar (stage cut < 1 %) to membranes of **SBAD-1**. Membranes were prepared by spincoating 0.5 mL of a 0.3 wt% polymer solution in tetrahydrofuran onto crosslinked Matrimid® supports. The polymer solution was aliquoted onto the center of the support spinning at a speed of 1000 rpm for 60 seconds after which, the procedure was repeated to generate a '2-layer' film. 2) A 10-component mixture containing 1 mol% each of select hydrocarbons listed as components 7-15 in Table S4 in toluene. The mixture was supplied at 30 bar and a flow rate of 1 L•min⁻¹ (stage cut < 1%) to circular coupons cut out from roll-to-roll coated membrane sheets. An **SBAD-1** solution was prepared at 0.8 wt% in chloroform and filtered through 200nm PTFE (FGLP04700, Merk) filters. Thin film composites were then prepared by coating onto crosslinked polyetherimide supports (average pore size: 9nm) via a roll-to-roll process line (RK Print, UK) as described elsewhere (8) at a casting speed of 5m/min and a drying temperature of 55 °C in an air-convection dryer. The rejection of molecules was correlated with aromaticity and molecular weight (Fig. S22). The same mixtures were used to test commercial Puramem® 280 membranes (Fig. 2C).

To prepare a membrane module of **SBAD-1** (Fig. S23), membranes (prepared through roll-to-roll processing as described above) were soaked in a solution of PEG400-IPA (1:1) for 24h then dried at room temperature until all IPA was removed. A membrane sheet (dimensions 0.3m x 1.7m) was cut from the prepared membrane roll, laid out, and folded in half with the coating layer facing inward. A sheet of feed spacer from Top Zeven, Netherlands (Polypropylene 2680, 28 mil thickness) was then placed between the folded membrane sheet. The permeate spacer from Sefar, Switzerland (PROPYLTEX 05-210/32, 295 μm thickness) was then attached to a perforated tube. Next, the “membrane-feed spacer-membrane sandwich” was glued on three sides at 70 °C forming an envelope open to the permeate tube. The solvent-stable glue designated EMET0001 was purchased from Evonik MET Limited (UK). After the envelope was completely wrapped around the permeate tube, extra glue was pasted along the straps on the outer surface of the roll to keep the spiral configuration and prevent unwrapping. The final rolled modules were approximately 0.0457 m in diameter and 0.3048 m long (1.8" \times 12"). Each module was made up of one membrane leaf ($\sim 0.4\text{m}^2$, $\sim 1.5\text{ m} \times \sim 0.25\text{ m}$) resulting in an effective area of $\sim 0.2\text{ m}^2$.

A complex, multicomponent mixture of 9 hydrocarbons (compositions detailed in Table S5) was used as a feed to determine the separation of a model crude oil fraction by **SBAD-1** thin film composite coupons and modules (both on crosslinked PEI support as described above, Fig. S24) at 40 bar under cross flow. The stage cut was maintained below 1% and separation factors for a component pair, A-B, were calculated as:

$$\text{Separation Factor}_{A/B} = \frac{C_{A,P}}{C_{A,R}} \cdot \frac{C_{B,R}}{C_{B,P}} \quad (6)$$

where $C_{A,P}$ and $C_{A,R}$ are the permeate and retentate compositions of component A and $C_{B,P}$ and $C_{B,R}$ are the permeate and retentate compositions of component B.

The impact of pressure and temperature variation on the separation of the 9-component model crude mixture was tested. A coupon of **SBAD-1** was loaded into a stainless steel cross-flow cell. The cell was placed into a custom-built cross-flow system equipped with feed and recirculation pumps, back-pressure regulators on permeate and retentate lines, a hot-box purged with nitrogen to maintain uniform temperature and automated permeate and retentate sampling system. A constant feed-rate of 300 mL/hr was maintained under full-recycle, i.e. permeate and retentate were recycled back to the feed container. The retentate back-pressure regulator was initially set to 45 bar while permeate was maintained at atmospheric pressure. The hot-box temperature was initially set to 25°C. Permeate and retentate samples were collected every 24 hours and analyzed by gas chromatography. After steady-state was achieved (no change in permeate and retentate composition), the hot-box temperature was increased to 35°C. This process was repeated at 50°C and 75°C. This set of experiments at four temperatures was repeated at 50 bar and 55 bar retentate pressures. Fig. S25 validates the increase of separation factors with increasing pressure as is generally observed in OSN. However, the separation factors were independent of temperature except when the performance suffered at a much higher temperature (75 °C). Recycling the membrane back to 35°C and 45 bar after treatment at 55 bar increased the separation performance, which could be due to slow temporal changes in transport rates through the membrane (Fig. S25B). Ultimately, this shows that the high temperatures and pressures did not damage the membrane and cause permanent loss in performance.

Batch separation of whole crude using SBAD-1

A 49 mm diameter coupon of **SBAD-1** was loaded into a Sterlitech HP4750X stirred dead-end cell (active membrane area = 14.6 cm²) with a custom-made heating jacket and nitrogen line for application of head pressure. The cell was initially loaded with 50g of toluene which was allowed to permeate overnight at room temperature and 800 psig N₂ head pressure. The cell was then depressurized and loaded with 100 g of shale-based light whole crude oil and 800 psig N₂ head pressure was again applied. The cell was stirred at a constant rate of 400 rpm. A cold trap cooled by dry ice was set up to collect the permeate in order to prevent loss of the light ends. The temperature of the cell was slowly increased up to 130°C until permeate flow was observed. After sufficient permeate had been collected, the cell was cooled and depressurized. The permeate, retentate and feed samples were analyzed using simulated distillation (SIMDIS) and 2-dimensional gas chromatography (GCxGC).

The GCxGC system consisted of an Agilent 6890 gas chromatograph (Agilent Technologies, Wilmington, DE) configured with a split/splitless inlet, oven, and flame ionization detector, and a Zoex ZX1 looped jet thermal modulation assembly (Zoex Corp., Houston, TX). The column system was a combination of three different columns connected in series. The first column was a weakly-polar BPX-5 (30 m length, 0.25 mmID, 0.25 μm film), followed by an intermediate-polarity BPX-50 (1.5 m length, 0.1 mmID, 0.1 μm film) interface column, and an additional intermediate-polarity BPX-50 (1.9 m length, 0.1 mmID, 0.1 μm film) analytical column. All columns were purchased from SGE Analytical (SGE Analytical Science, Austin, TX). The ZX1 modulator uses a combination of alternating cold and hot nitrogen gas jets regulated by liquid nitrogen heat-exchange and electric auxiliary heating to trap and release “slices” of eluent from the first column onto the second column. This trapping occurs on the interface column which is looped through the intersection of both gas jets in the oven.

A 2.0 μL sample was injected neat into the split/splitless inlet with a 20:1 split ratio at 360°C. The carrier gas was helium running in constant flow mode at 1.9 mL per minute. The oven was programmed from 60°C to 390°C at 3°C per minute for a total run time of 110 minutes. The modulator hot jet is programmed from 180°C to 390°C at 3°C per minute and then held for 40 minutes until the end of the run. The modulation period was 10 s with a hot jet pulse length of 400 ms. The FID sample rate was 100 Hz. Instrument control and FID data collection was conducted using Agilent Chemstation.

FID signal processing was conducted using GC Image software (GC Image, LLC, Lincoln, NE). GC Image constructed the two-dimensional and three-dimensional GCxGC plot images from the Chemstation FID channel file using built-in baseline correction, peak detection, and peak integration algorithms. Three-dimensional comparison images were also constructed using built-in functionality.

GCxGC chromatograms were split according to molecular class (normal paraffins, branched paraffins, naphthenes and aromatics) and normalized cumulative peak volume was plotted against retention time for both feed and permeate for each class. A polynomial (depending on goodness of fit) was fit to each curve and integrated between the limits of lowest and highest retention time to obtain the area under the curve (n-paraffins example shown in Fig. S26). For each class, the area under the normalized cumulative peak volume curve for the feed was subtracted from that for the permeate. This difference in area was then expressed as a percentage of the area under feed curve to obtain the “% enrichment” of each class in the permeate relative to the feed (Table S7).

For calculation of class-wise rejection, the peak volumes for each class were binned into 5-minute retention time intervals for both feed and permeate. The rejection at a given retention time

was then calculated as shown in Equation 5 where C_p is the peak volume of permeate and C_f is the peak volume of feed at the same retention time. The rejection curves for each class as well as total rejection were then plotted against retention time (Fig. S27).

Table S1. Conditions tested for the polymerization of **SBAD-1: 1** (0.1 mmol), diamine (0.1 mmol), catalyst (5 mol%), solvent (0.5 mL) for 24h. Reaction 2 was performed at 0.1 M (1 mL dioxane) to prevent gelation.

Entry	Catalyst	Temp. (°C)	Solvent	M _w (kDa)
1	P1-L1	50	Dioxane	No Conv
2	P2-L1	100	Dioxane*	16.7
3	P2-L1	50	Dioxane	80.4
4	L1•Pd(dba) ₂	50	Dioxane	8.0
5	L2•Pd(dba) ₂	50	Dioxane	4.2
6	P2-L1	140	DMAc	25.5
7	P2-L3	50	Dioxane	1.4
8	P1-L3	110	Toluene	9.3
9	P2-L1	110	Toluene	8.8
10	P2-L1	50	THF	113
11	L4•[PhCN] ₂ PdCl ₂	110	Toluene	2.3
12	L4•[PhCN] ₂ PdCl ₂	100	Dioxane	4.6

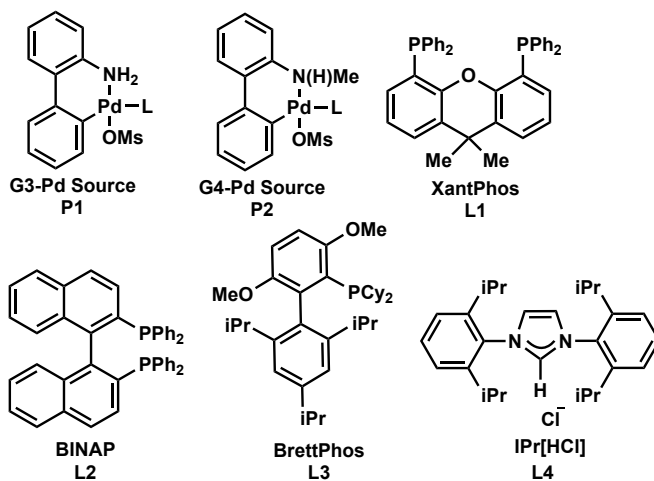




Fig. S2. Solutions of polymers in the **SBAD** series in chloroform (0.4 mg/mL).

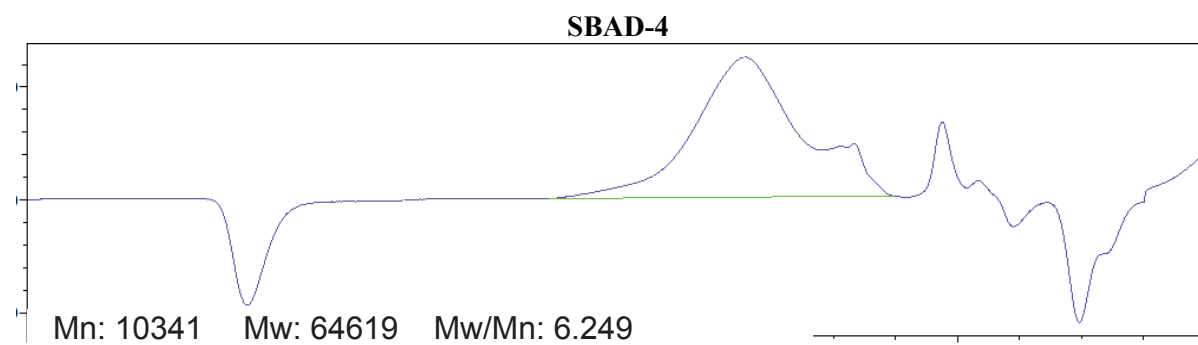
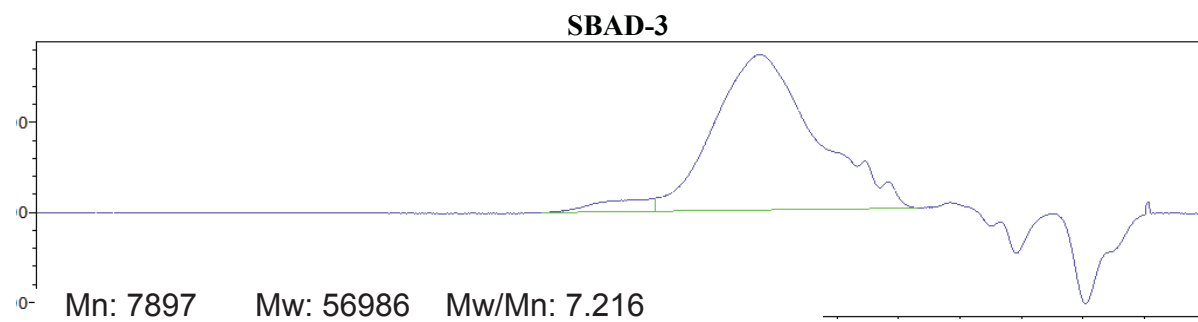
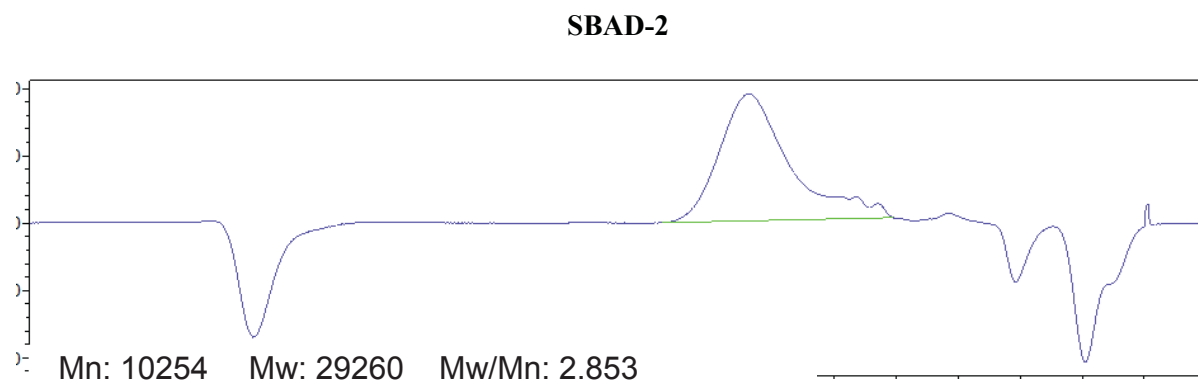
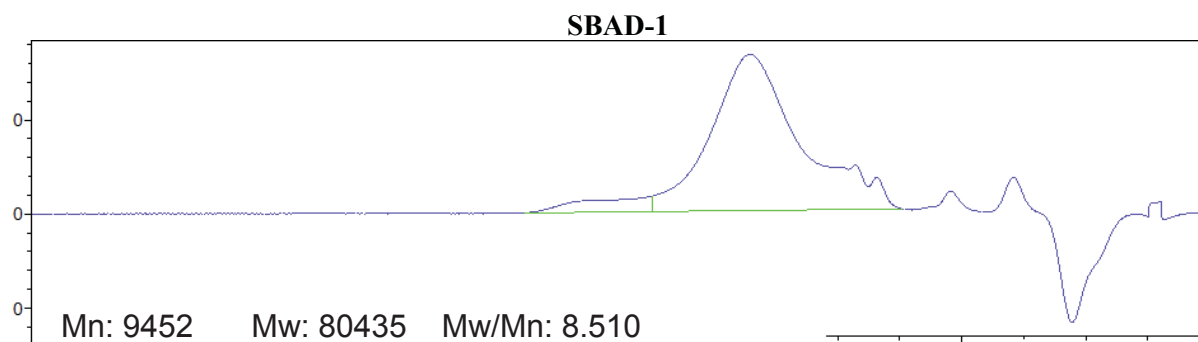


Fig. S3. GPC analyses of **SBAD** polymers.

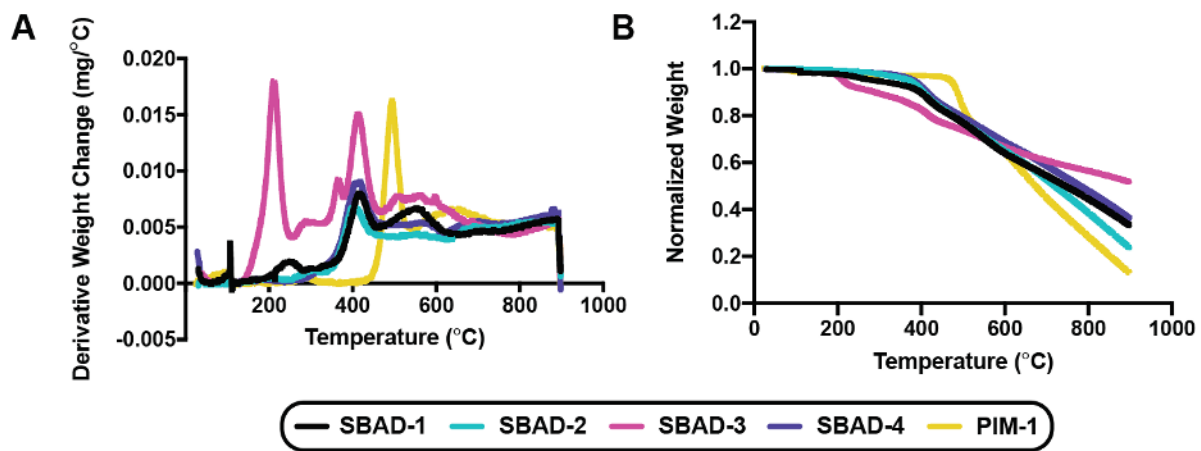


Fig. S4. Thermogravimetric analysis (TGA) of all polymers in the **SBAD** series compared to **PIM-1** shown as A) derivative weight change and B) weight normalized to starting sample weight.

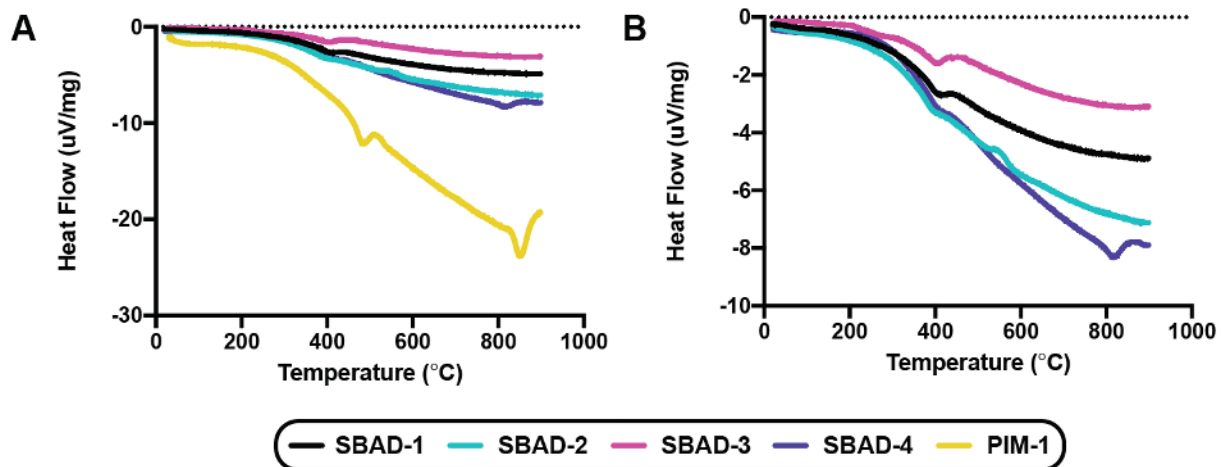


Fig. S5. Differential scanning calorimetry (DSC) of polymers in the **SBAD** series compared to **PIM-1**. Glass transition states were not observed below the decomposition temperatures observed in Fig. S4.

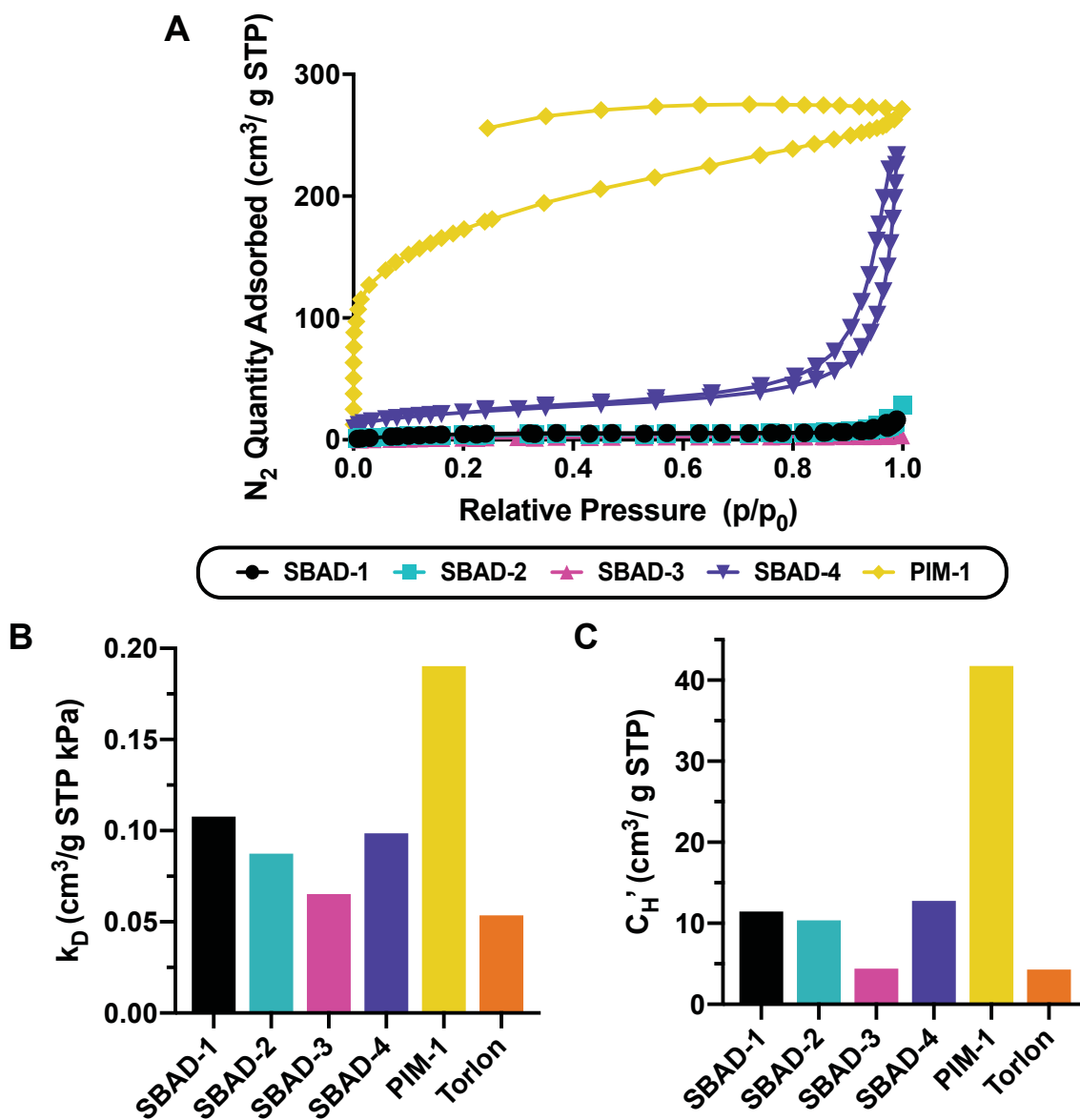


Fig. S6. Uptake of (A) N₂ (at 77 K) by **SBAD** polymers compared to **PIM-1**. (B) Henry's law coefficient (k_D) and (C) Langmuir capacity constant (C'_H) values fit to CO₂ sorption data, compared to data obtained for a traditional “non-porous” polymer, Torlon[®]. Error for k_D and C'_H were too small to be apparent on the graphs. Inset = key for panel A.

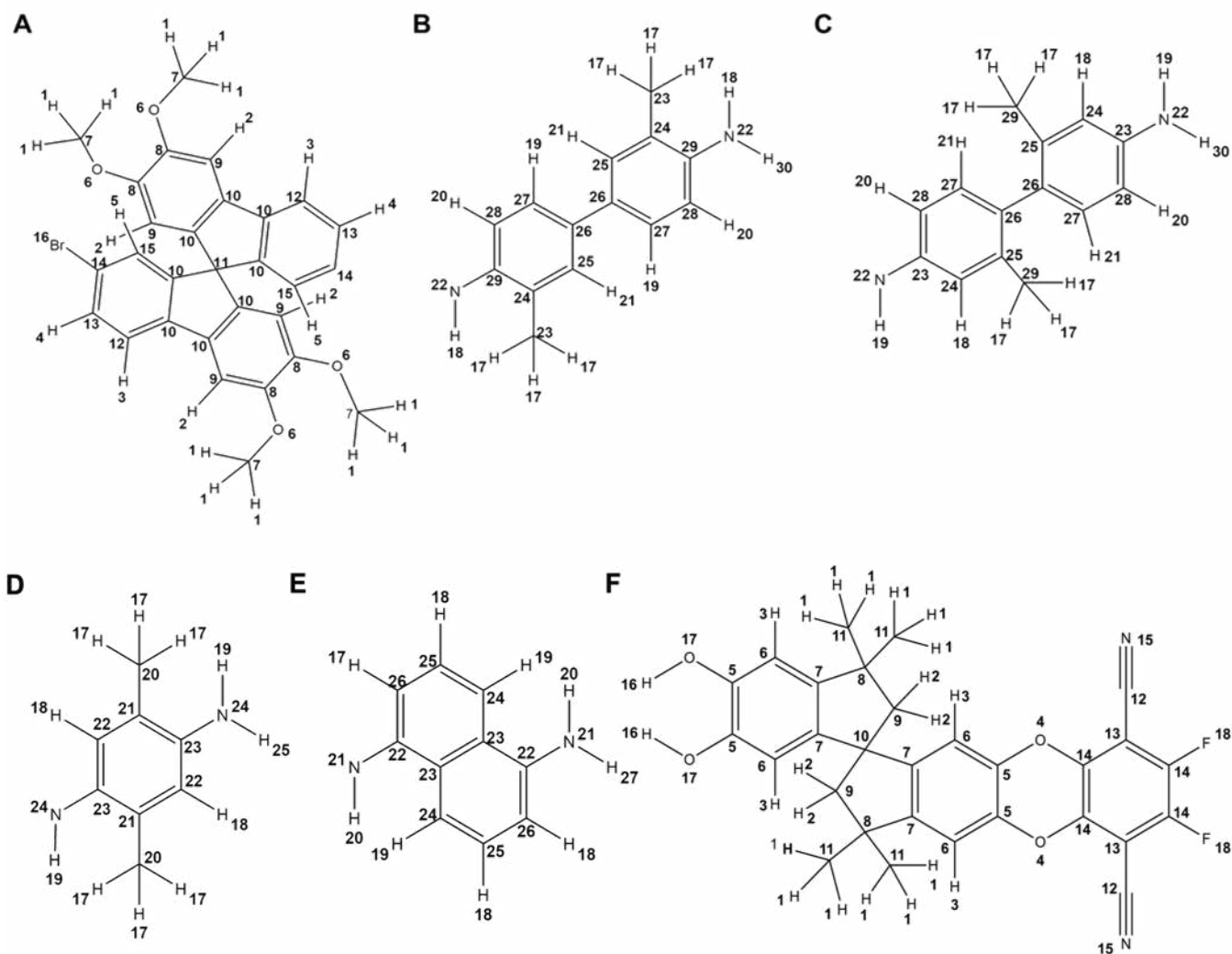


Fig. S7. Representation of the polymer monomers used for building the polymer models, with labelled atoms. A) monomer A for all the **SBAD** family polymers B-E) monomer B for **SBAD-1-4**. F) **PIM-1** monomeric unit.

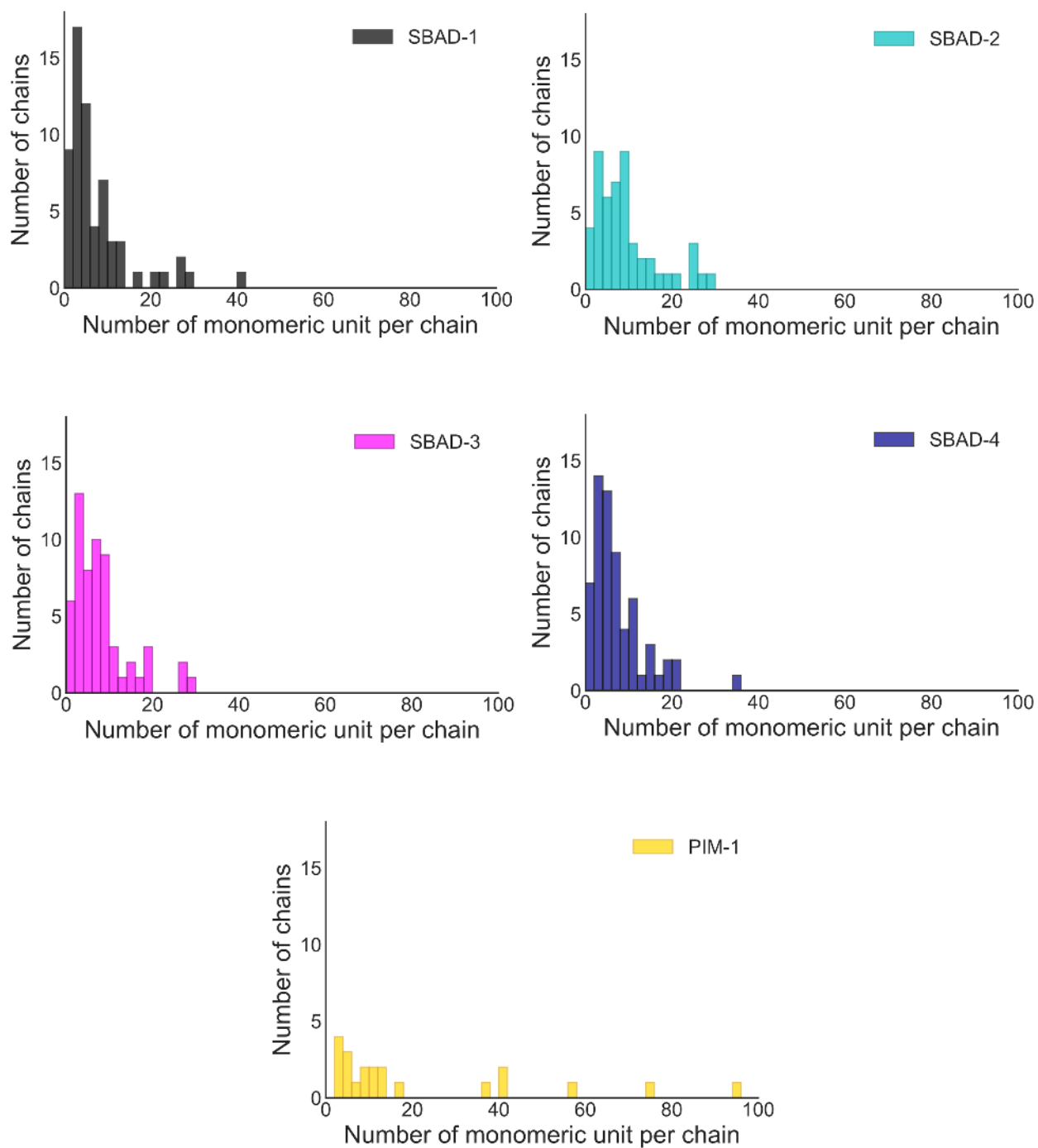


Fig. S8. Chain length distribution in the polymer models.

Table S2. Force field atom type and partial charges assigned to the atoms in the models. Monomer and atoms labels refer to the ones reported in Fig. S7.

SBAD-1	A	type	charge	B	type	charge	SBAD-2	A	type	charge	C	type	charge
	1	hc	0.0451	17	hc	0.1010		1	hc	0.0591	17	hc	0.1360
	2	hc	0.1631	18	hn	0.3803		2	hc	0.1592	18	hc	0.2510
	3	hc	0.1438	19	hc	0.1758		3	hc	0.1415	19	hn	0.2805
	4	hc	0.1531	20	hc	0.1896		4	hc	0.1505	20	hc	0.2389
	5	hc	0.1545	21	hc	0.1982		5	hc	0.1769	21	hc	0.1888
	6	oc	-0.3543	22	nb	-0.6420		6	oc	-0.3317	22	nb	-0.7447
	7	c	0.0360	23	c	-0.2702		7	c	-0.0317	23	cp	0.5588
	8	cp	0.2171	24	cp	0.1564		8	cp	0.2210	24	cp	-0.5845
	9	cp	-0.2612	25	cp	-0.3461		9	cp	-0.2572	25	cp	0.3582
	10	c5	-0.0281	26	cp	0.1172		10	c5	-0.0344	26	cp	-0.1866
	11	c	0.3471	27	cp	-0.2389		11	c	0.3878	27	cp	-0.0239
	12	cp	-0.1434	28	cp	-0.2165		12	cp	-0.1699	28	cp	-0.4375
	13	cp	-0.3561	29	cp	0.1932		13	cp	-0.3310	29	c	-0.3069
	14	cp	0.4020	30	hn	0.3767		14	cp	0.4341	30	hn	0.3708
	15	cp	-0.2871					15	cp	-0.3320			
16	br	-0.1075				16	br	-0.1070					
SBAD-3	A	type	charge	D	type	charge	SBAD-4	A	type	charge	E	type	charge
	1	hc	0.0569	17	hc	0.0905		1	hc	0.0584	17	hc	0.1923
	2	hc	0.1572	18	hc	0.2155		2	hc	0.1720	18	hc	0.1780
	3	hc	0.1483	19	hn	0.3814		3	hc	0.1548	19	hc	0.1429
	4	hc	0.1342	20	c	-0.1739		4	hc	0.1643	20	hn	0.3423
	5	hc	0.1595	21	cp	0.0775		5	hc	0.1673	21	nb	-0.5284
	6	oc	-0.3323	22	cp	-0.3398		6	oc	-0.3424	22	cp	0.2257
	7	c	-0.0184	23	cp	0.2056		7	c	0.0031	23	cp	0.0309
	8	cp	0.2164	24	nb	-0.6378		8	cp	0.2097	24	cp	-0.1780
	9	cp	-0.2529	25	hn	0.3760		9	cp	-0.2562	25	cp	-0.1504
	10	c5	-0.0391					10	c5	-0.0034	26	cp	-0.2553
	11	c	0.4147					11	c	0.1675	27	hn	0.3724
	12	cp	-0.1968					12	cp	-0.2319			
	13	cp	-0.2707					13	cp	-0.2860			
	14	cp	0.3943					14	cp	0.3038			
	15	cp	-0.3010					15	cp	-0.2648			
16	br	-0.1090				16	br	-0.1182					
PIM-1	A	type	charge	F	type	charge	A	type	charge	F	type	charge	
	1	hc	0.0838	10	c	0.5258	6	cp	-0.3575	15	nt	-0.4895	
	2	hc	0.0801	11	c3	-0.3917	7	cp	-0.1007	16	ho	0.4725	
	3	hc	0.2104	12	ct	0.5108	8	c	0.6236	17	oh	-0.2992	
	4	oc	-0.2992	13	cp	-0.3224	9	c2	-0.4149	18	f	-0.1437	
5	cp	0.2787	14	cp	0.2472								

Table S3. Characterization of the amorphous polymer models for the four **SBAD** polymers and **PIM-1**. For each polymer, results are averaged over three independent models deriving from different initial random packing. The standard deviation is reported in parenthesis. The diameters of the largest included sphere (D_I), largest free sphere (D_F) and largest included sphere along the free sphere path (D_{IF}) are reported, as well as the surface area (SA) with different diameter probes.

	SBAD-1	SBAD-2	SBAD-3	SBAD-4	PIM-1
Initial packing density (g·cm³)	0.381	0.381	0.396	0.429	0.334
% of polymerization reached	93.1 (0.9)	94.8 (0.9)	93.5 (0.7)	93.0 (0.7)	95.3 (0.7)
No. of bonds formed	279 (3)	283 (3)	280 (2)	279 (2)	143 (1)
Final bulk density (g·cm³)	1.052 (0.007)	1.045 (0.008)	1.002 (0.004)	1.080 (0.005)	0.999 (0.029)
No. chains in the model	21 (3)	17 (3)	20 (2)	21 (2)	7 (1)
D_I (Å)	6.64 (0.76)	7.95 (1.16)	6.83 (0.39)	7.57 (1.74)	10.53 (1.70)
D_F (Å)	2.30 (0.08)	2.30 (0.13)	2.28 (0.02)	2.23 (0.03)	3.18 (0.34)
D_{IF} (Å)	6.21 (1.11)	6.97 (0.62)	6.16 (0.65)	7.24 (1.85)	9.18 (1.93)
SA (2.00 Å probe) cm²·g⁻¹	1381 (31)	1455 (17)	1498 (30)	1361 (33)	1959 (48)
SA (2.20 Å probe) cm²·g⁻¹	1073 (29)	1147 (14)	1183 (34)	1063 (40)	1687 (57)
SA (3.30 Å probe – CO₂) cm²·g⁻¹	232 (18)	277 (11)	278 (32)	235 (52)	717 (77)
SA (3.64 Å probe – N₂) cm²·g⁻¹	138 (15)	175 (7)	171 (24)	143 (48)	550 (81)

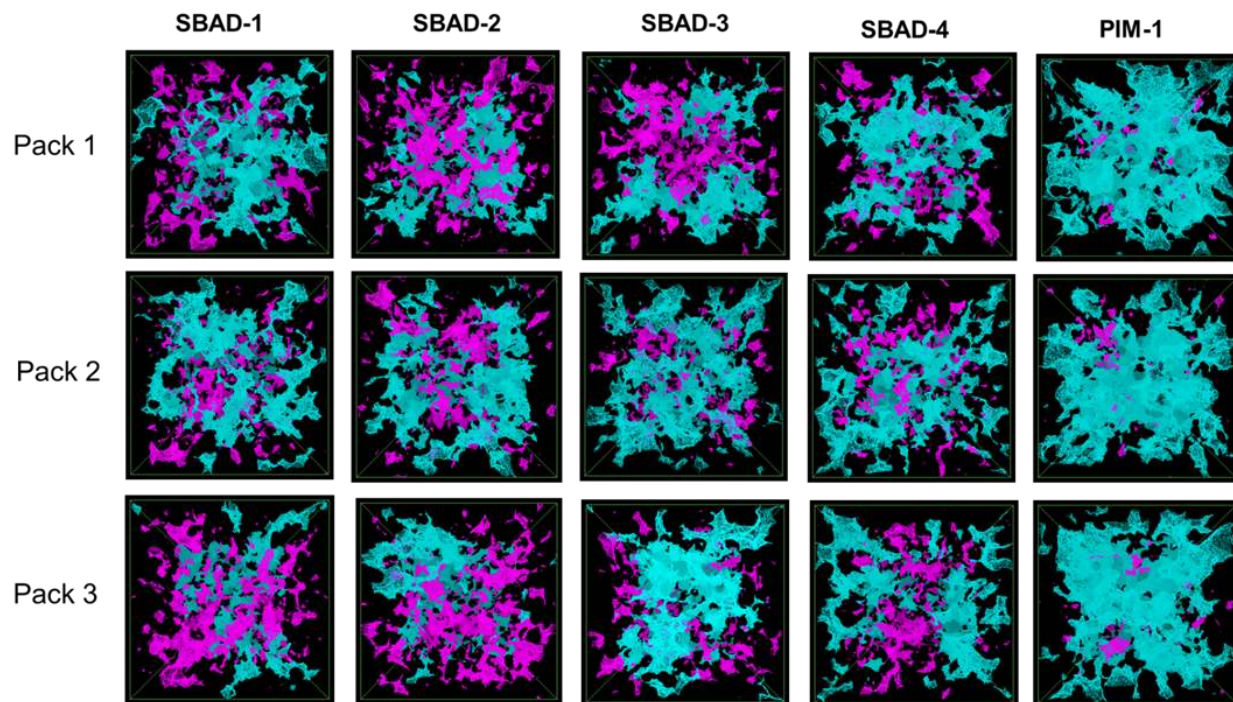


Fig. S9. Accessible (teal) and non-accessible (magenta) surface area for all polymers in the **SBAD** series compared to **PIM-1** using a 2.2 Å probe diameter.

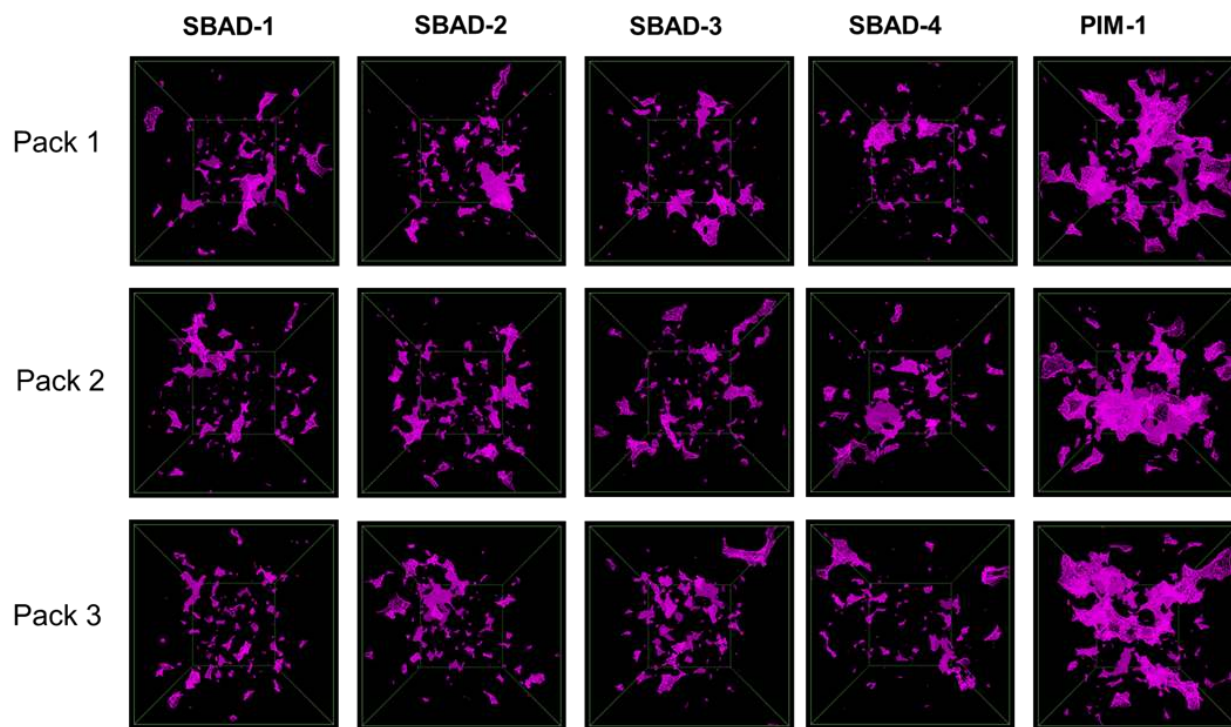


Fig. S10. Non-accessible (magenta) surface area for all polymers in the **SBAD** series compared to **PIM-1** using a 3.64 Å probe diameter (kinetic diameter of N₂).

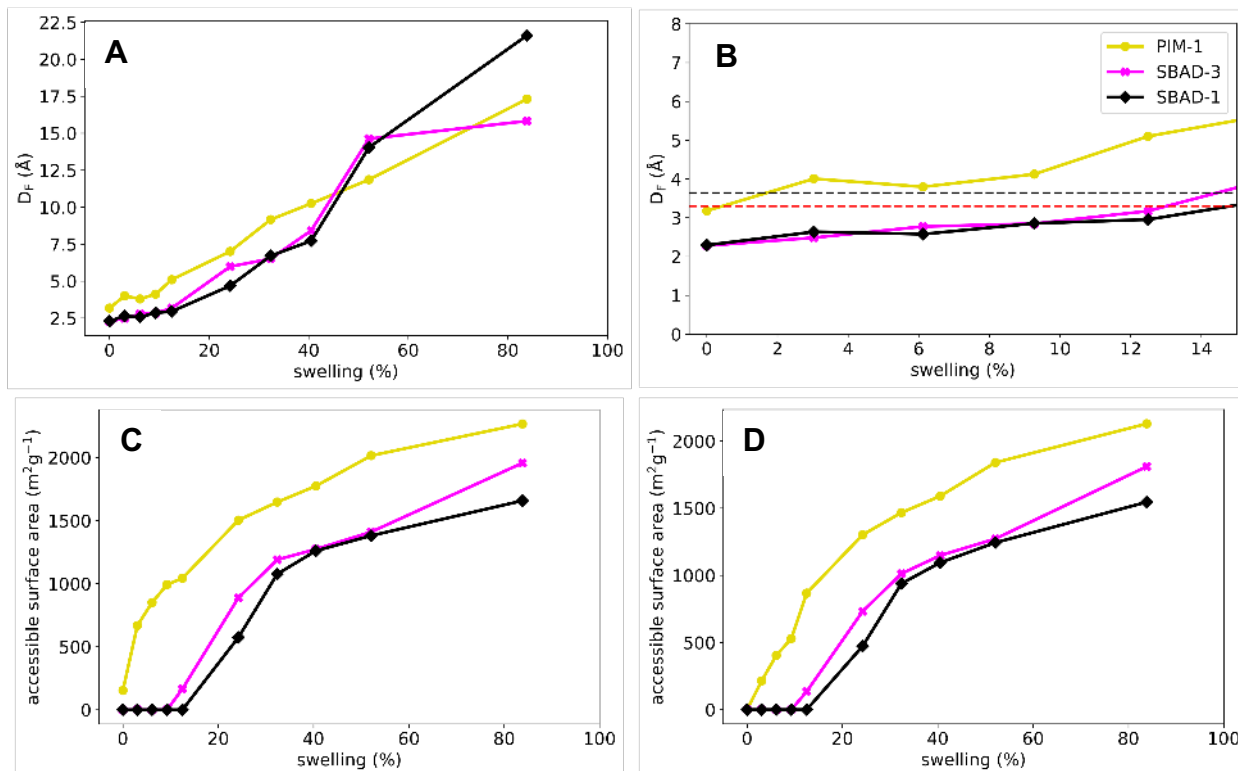


Fig. S11. (A)-(B) Average pore limiting diameter (D_F) of **PIM-1**, **SBAD-1** and **SBAD-3** as a function of swelling. In (B), the red and black dashed lines represent the probe diameter of CO_2 and N_2 , respectively. (C)-(D) The average solvent accessible surface area of **PIM-1**, **SBAD-1** and **SBAD-3** as a function of swelling for CO_2 (left) and N_2 (right) probes.

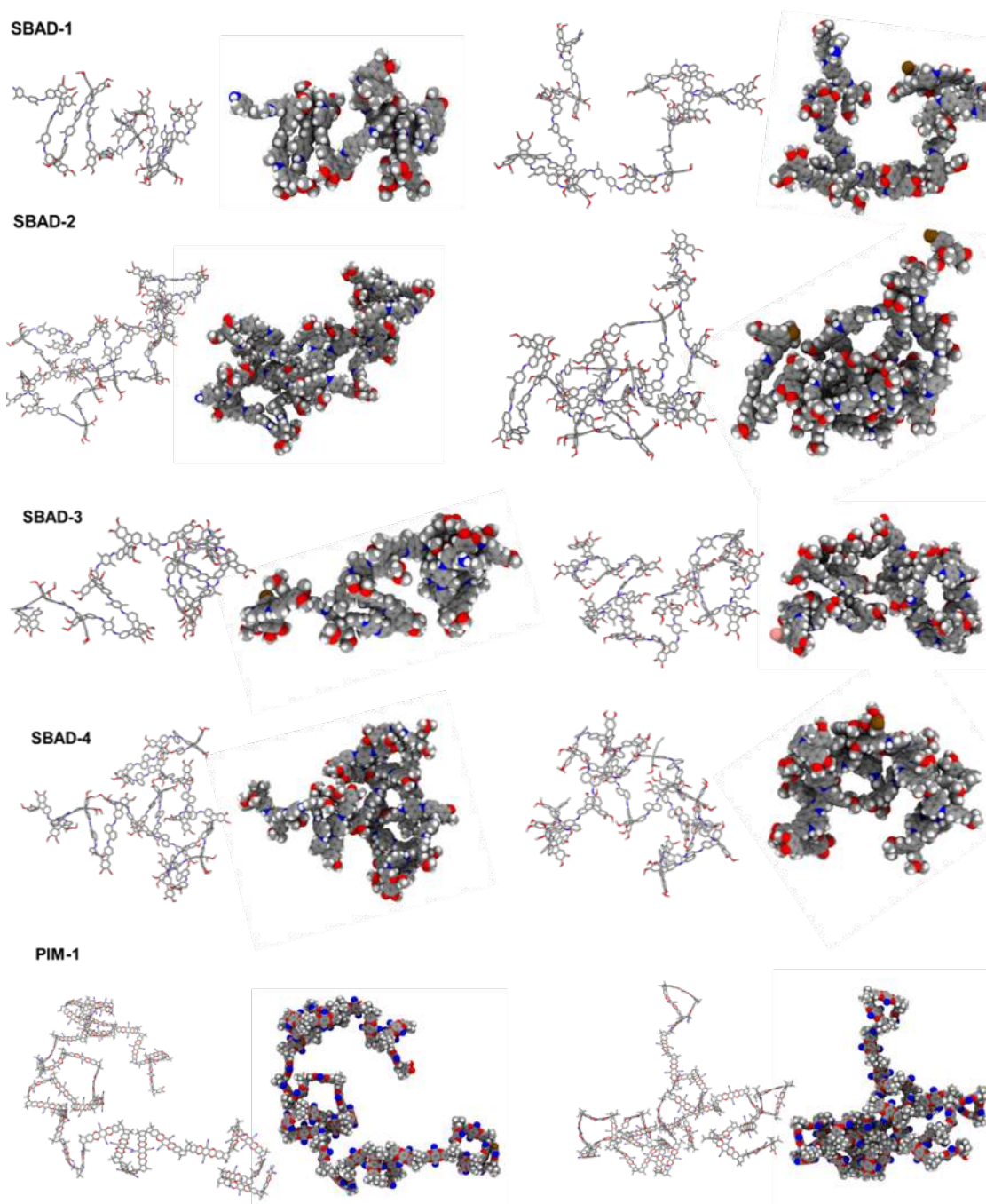


Fig. S12. Stick and space filling representations of two selected chains for each polymer. Hydrogens have been removed for clarity in the stick representation. Color code: carbon in grey, nitrogen in blue, oxygen in red, hydrogen in white, bromine in purple, fluorine in light blue.

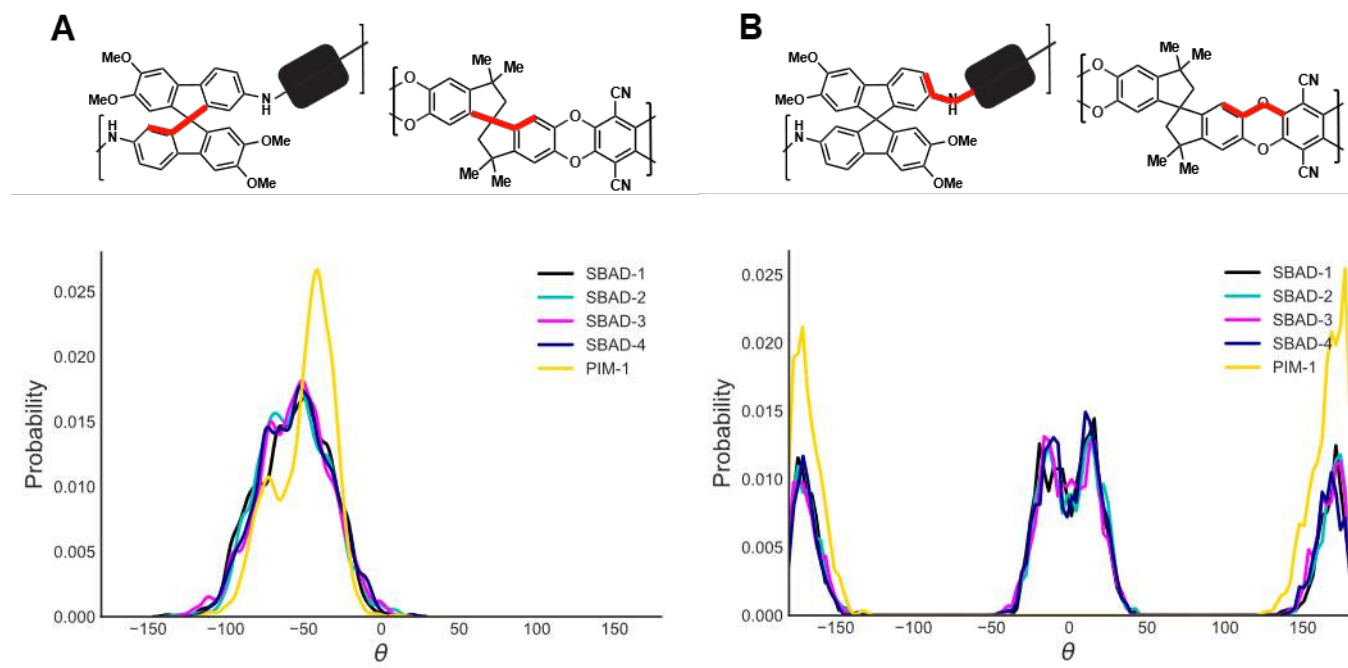


Fig. S13. Histograms of the angle distributions for the dihedral highlighted in red in the final models for the **SBAD** polymers and **PIM-1**. A) Dihedral angle involving the spirocenter B) dihedral angle involving the linkage between the two monomers.

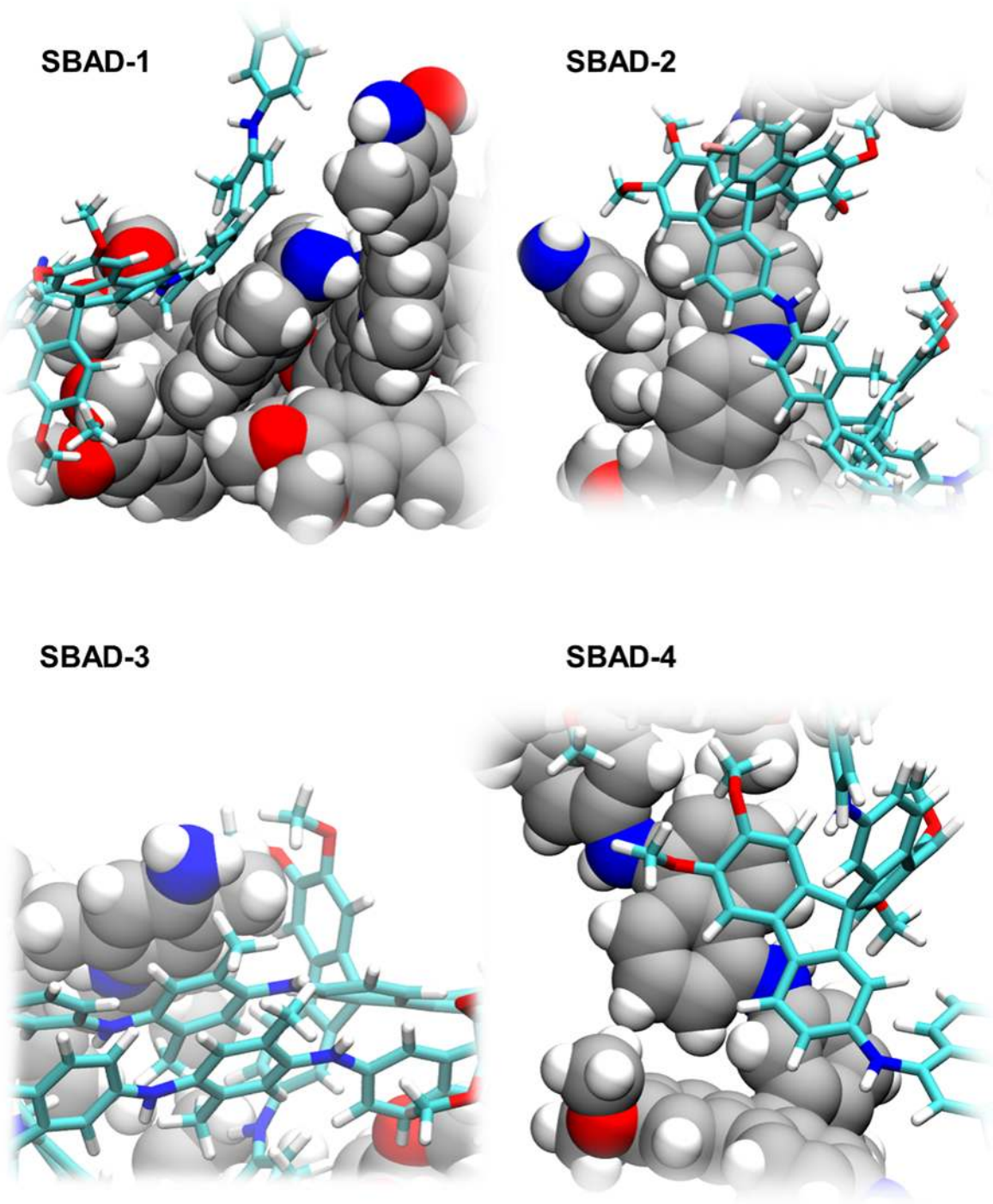


Fig. S14. Selected snapshots that highlight π - π stacking interactions between chains inside the polymer models of the **SBAD** family. One chain is shown in van der Waals representation with carbon in grey, the other is represented in stick with the carbons in light blue. Nitrogen is in blue, oxygen in red, hydrogen in white.

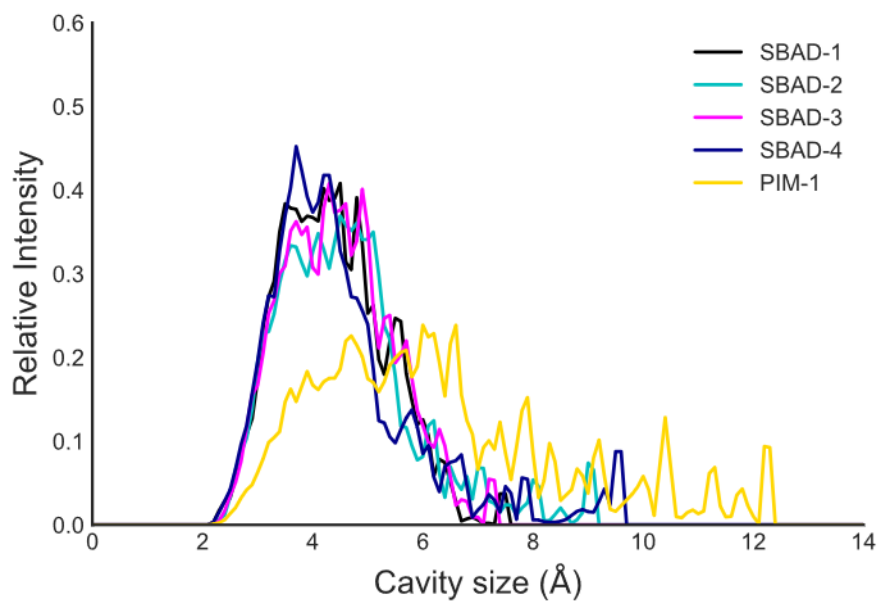


Fig. S15. Calculated pore size distribution of the **SBAD** series compared to **PIM-1**.

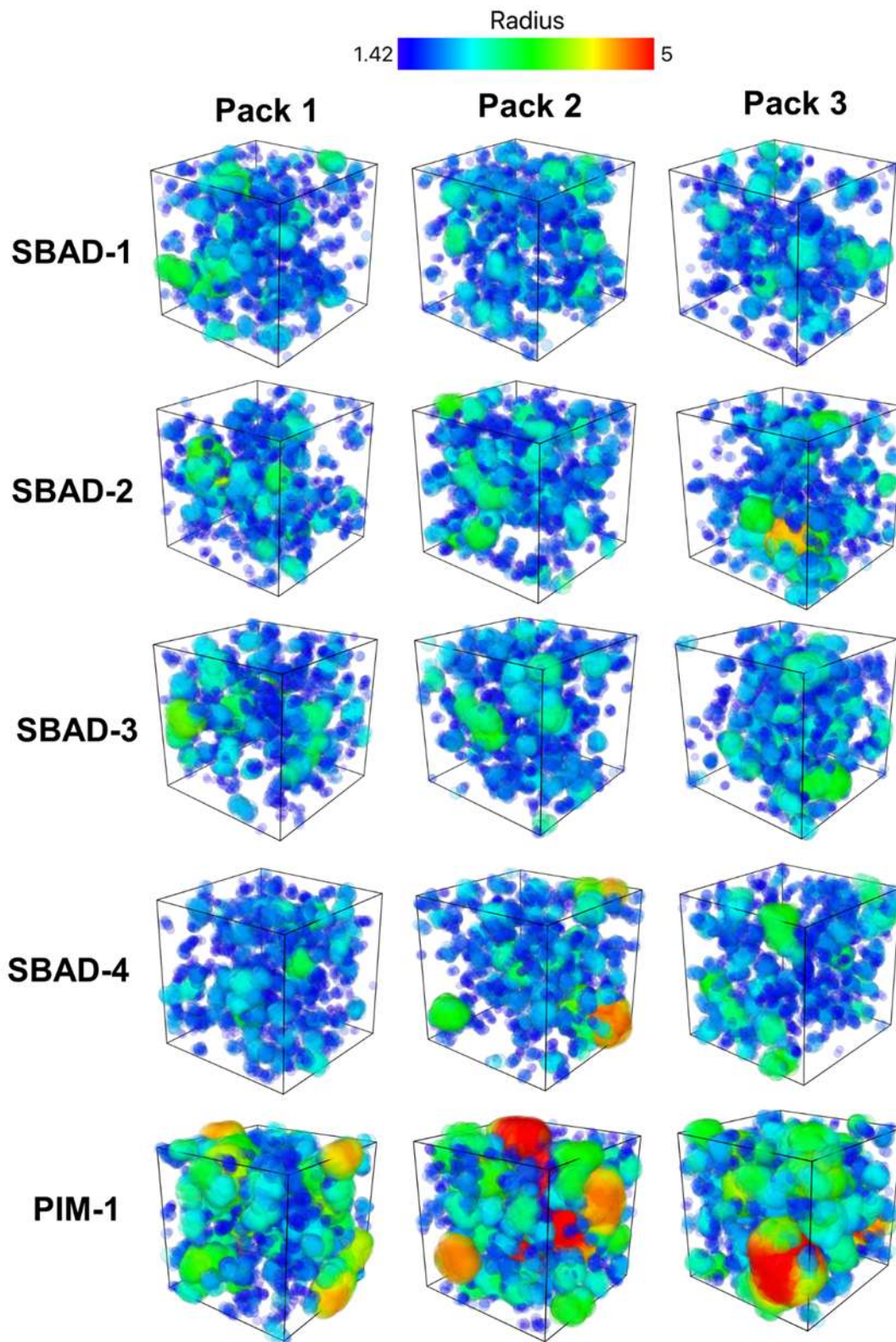


Fig. S16. Three-dimensional representation of the pore size distribution in the three models for each of the five polymers. Pores are color-coded based on their dimension. Only pores bigger than 1.42 Å radius are displayed.

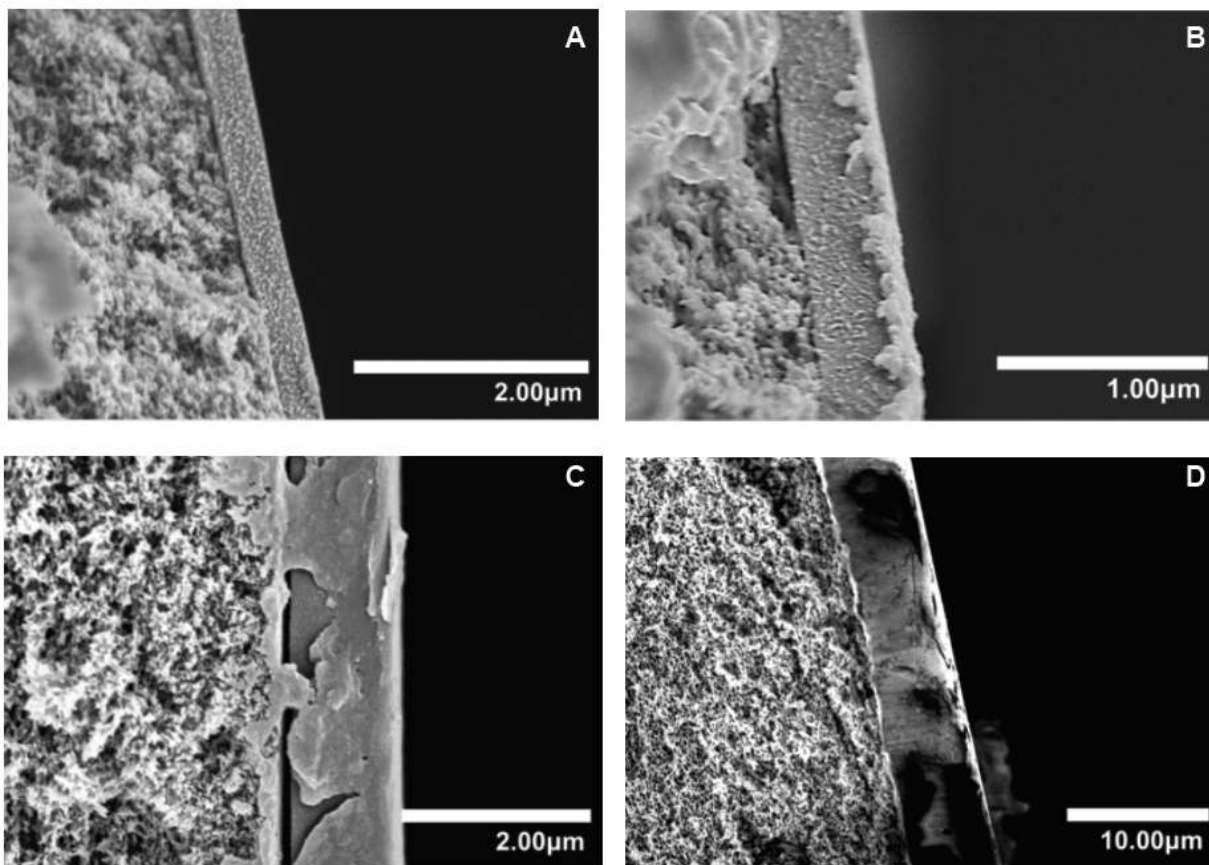


Fig. S17. Side view of thin film-composites: dense polymer layer coated on porous crosslinked polyetherimide. A) SBAD-2 B) SBAD-3 C) SBAD-4 D) PIM-1

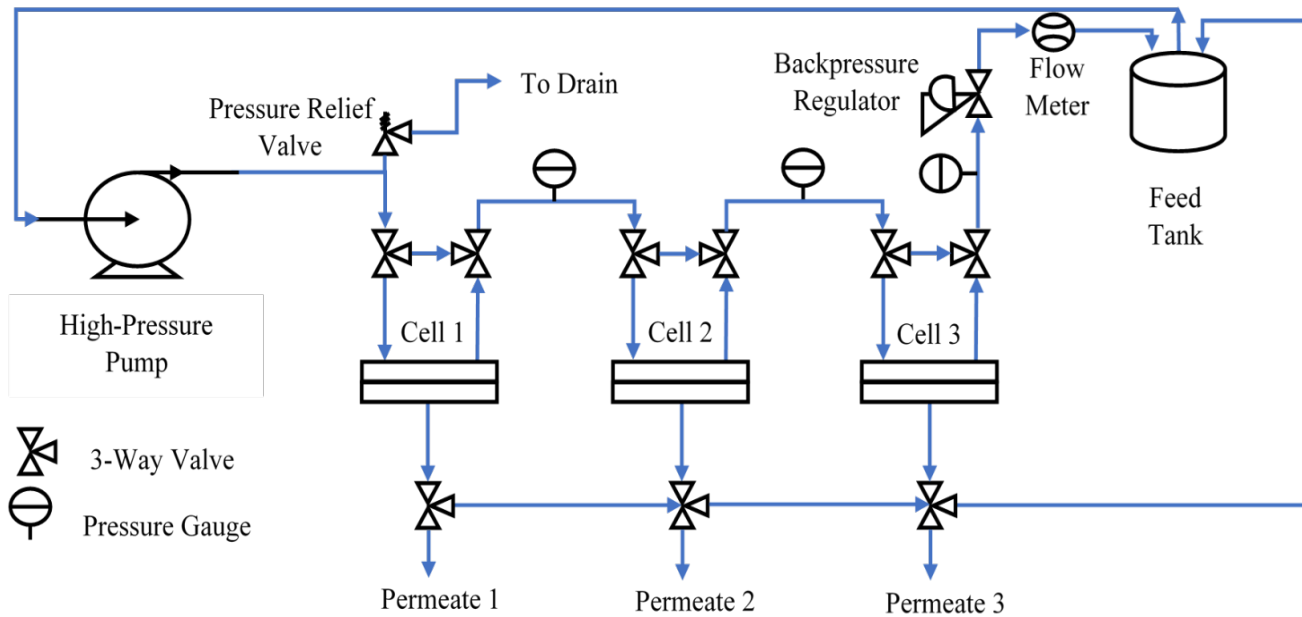


Fig. S18. Schematic of cross-flow permeation system.

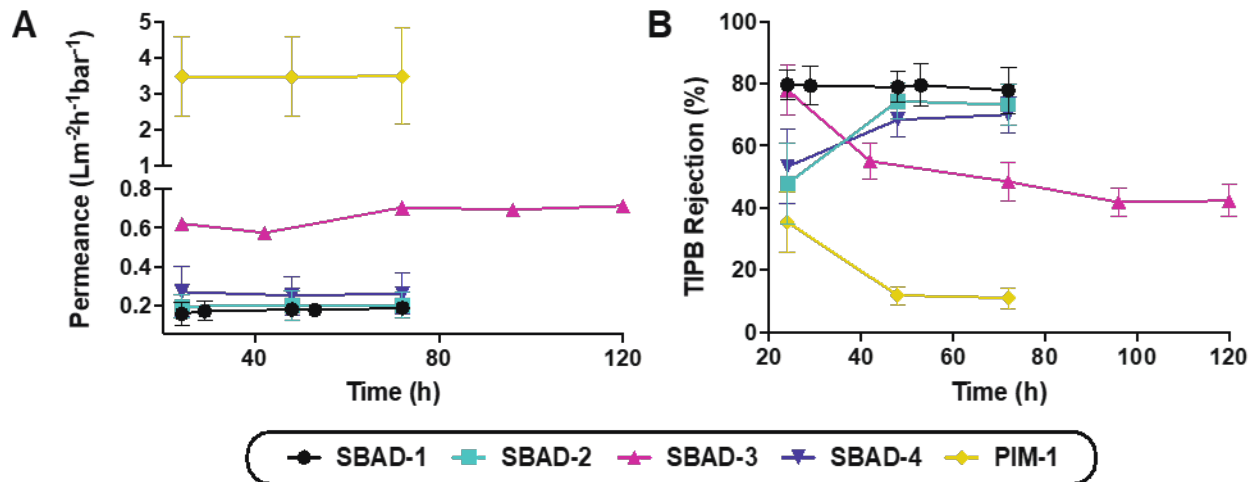


Fig. S19. Transient membrane performance showing (A) toluene permeance and (B) 1,3,5-triisopropyl benzene (TIPB) rejection of **SBAD** polymer membranes compared to **PIM-1**.

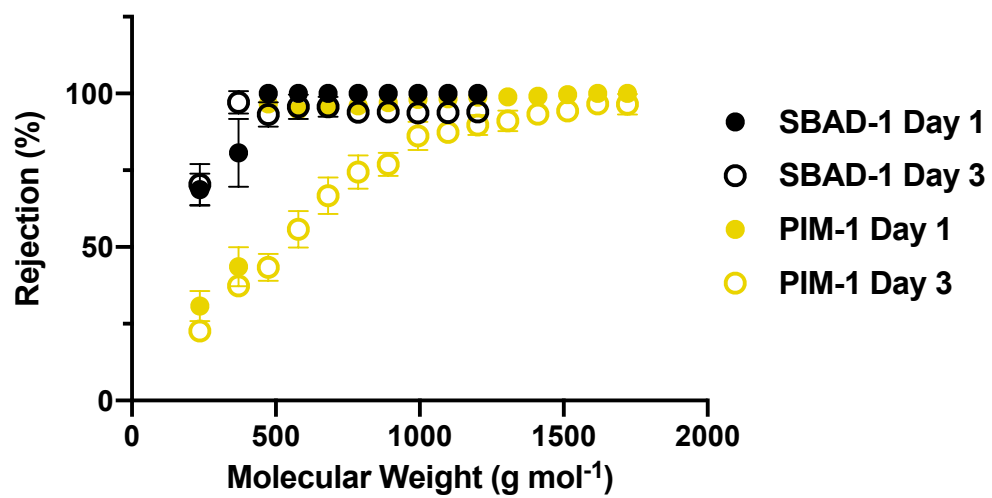


Fig. S20. Comparison of SBAD-1 and PIM-1 oligostyrene rejection over three days.

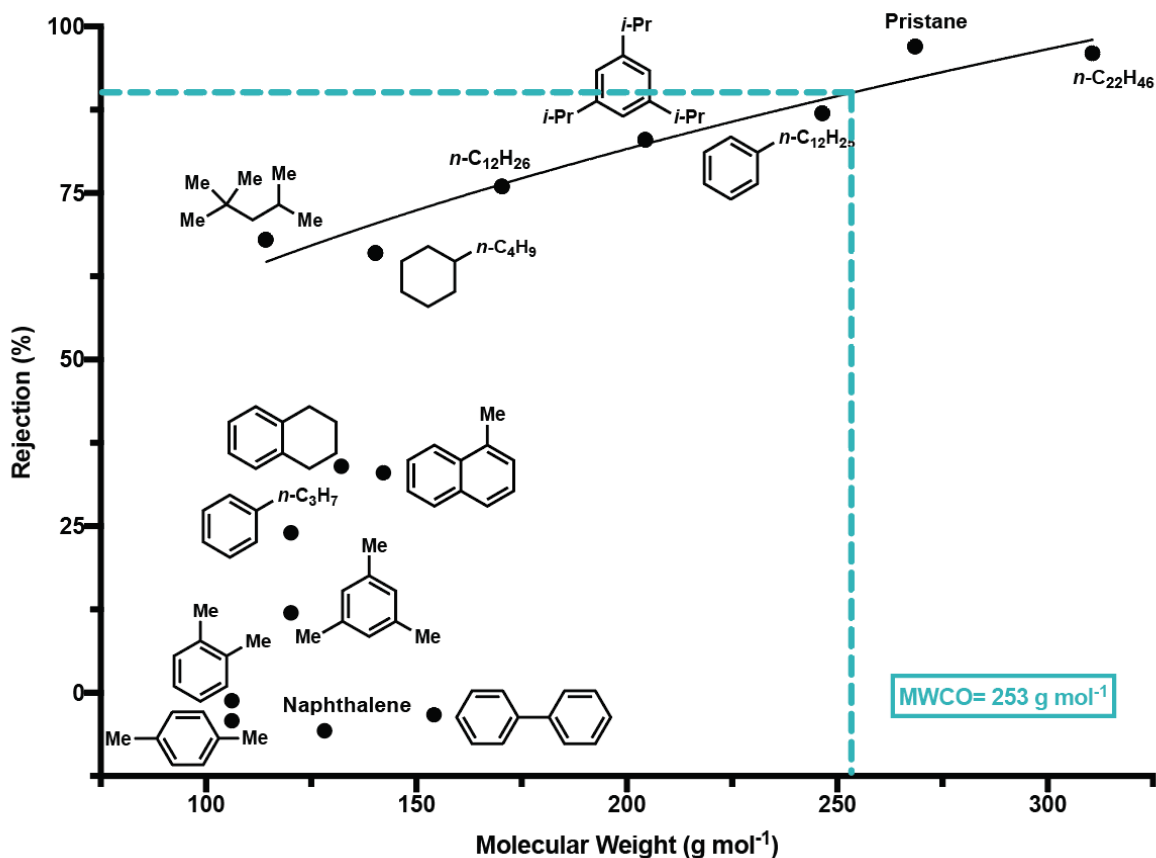


Fig. S21. Hydrocarbon molecular weight cutoff curve (threshold = 253 g·mol⁻¹) for SBAD-1 using a 1 mol% concentration of individual solutes of two the mixtures listed in Table S4. Cutoff was determined by fitting all data points above 60% rejection to a log/log curve (equation of curve: $10^{((\log(y)-0.9549)/0.4158)} = x$) and interpolating to 90% rejection.

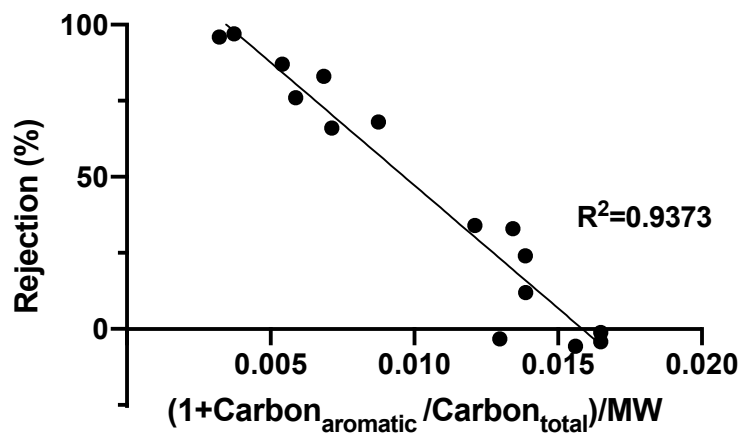


Fig. S22. Dependence of rejection on aromaticity and molecular weight (MW, g-mol⁻¹) where the effect of aromaticity (sorption) and molecular weight (diffusion) are coupled as represented by $(1 + \text{Carbon}_{\text{aromatic}} / \text{Carbon}_{\text{total}}) / \text{MW}$.

Table S4. Steady-state rejection of a 7-component mixture comprised of six solutes at 1 mol% in a dilute feed mixture in toluene tested at 10 bar over a 66-hour period for **SBAD-1** thin film composites formed via spin coating on Matrimid® supports; and steady-state rejection of a 10-component mixture comprised of 9 solutes included at 1 mol% in a dilute feed mixture in toluene tested at 30 bar over a 24-hour period for **SBAD-1** thin film composites formed via roll-to-roll coating on Ultem® supports. Puramem® 280 was tested under the same conditions as described above. The difference in permeance is likely due to differences in film thickness due to the method of production. Negative rejections indicate enrichment of the component in the permeate.

		<i>SBAD-1</i>	<i>Puramem®</i> <i>280</i>
7-comp mixture	<u>Species</u>	<u>MW (g·mol⁻¹)</u>	<u>Rejection (%)</u>
	p-xylene	106.17	-4.2 ± 0.9
	o-xylene	106.17	-1.3 ± 0.7
	mesitylene	120.19	12 ± 0.6
	naphthalene	128.17	-5.7 ± 1.4
	biphenyl	154.21	-3.3 ± 1.5
	1,3,5-triisopropylbenzene	204.36	83 ± 1.1
	Permeance (L·m⁻²·h⁻¹·bar⁻¹)		0.24 ± 0.05
10-comp mixture	isooctane	114.22	68 ± 0.7
	propylbenzene	120.20	23 ± 2.1
	tetralin	132.20	34 ± 1.1
	n-butylcyclohexane	140.27	66 ± 0.6
	1-methylnaphthalene	142.20	33 ± 0.4
	dodecane	170.33	75 ± 0.4
	dodecylbenzene	246.43	86 ± 0.7
	pristane	268.51	97 ± 1.3
	n-docosane	310.60	96 ± 1.2
	Permeance (L·m⁻²·h⁻¹·bar⁻¹)		0.15 ± 0.03

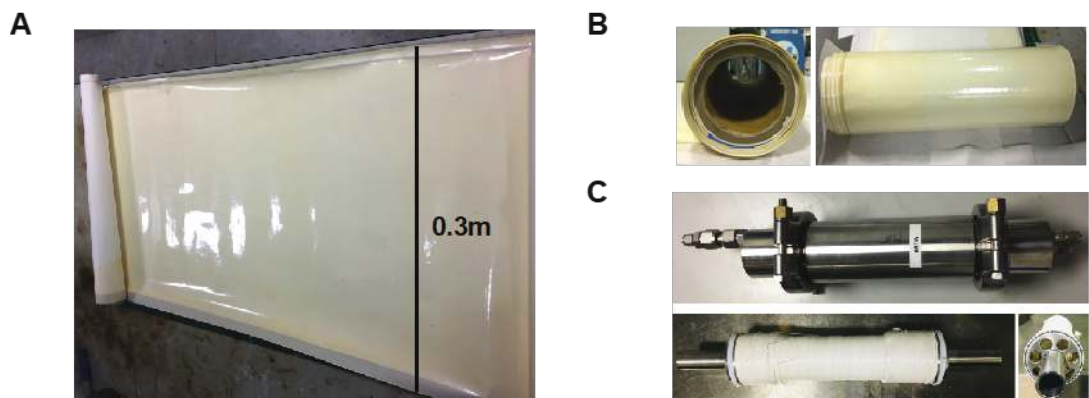


Fig. S23. (A) Thin film composite sheet of **SBAD-1** on Ultem®. (B) Scaled-up flat sheet membrane roll of **SBAD-1** prepared through roll-to-roll coating. (C) Spiral wound **SBAD-1** module comprised of 1.8 m x 0.2 m of membrane.

Table S5. 9-component feed mixture that was used as a model for the separation of a middle distillate cut of crude oil and the resulting ratios of concentration in permeate (C_P) over concentration in retentate (C_R) for both membrane coupons and a spiral wound module of **SBAD-1**.

	MW (g-mol ⁻¹)	Feed Concentration (mol%)	C_P/C_R	
			Coupon	Module
toluene	92.14	17	1.18 ± 0.02	1.09 ± 0.00
methylcyclohexane	98.19	28	0.90 ± 0.01	0.97 ± 0.02
<i>n</i> -octane	114.22	22	1.11 ± 0.02	0.98 ± 0.00
isooctane	114.22	15	0.82 ± 0.05	0.92 ± 0.02
<i>tert</i> -butylbenzene	134.21	2.2	1.25 ± 0.03	0.99 ± 0.00
decalin	138.25	11	1.03 ± 0.00	0.94 ± 0.01
1-methylnaphthalene	142.20	2.0	1.40 ± 0.05	1.06 ± 0.00
TIPB	204.35	1.6	0.52 ± 0.07	0.77 ± 0.00
isocetane	226.45	1.3	0.34 ± 0.06	0.73 ± 0.01

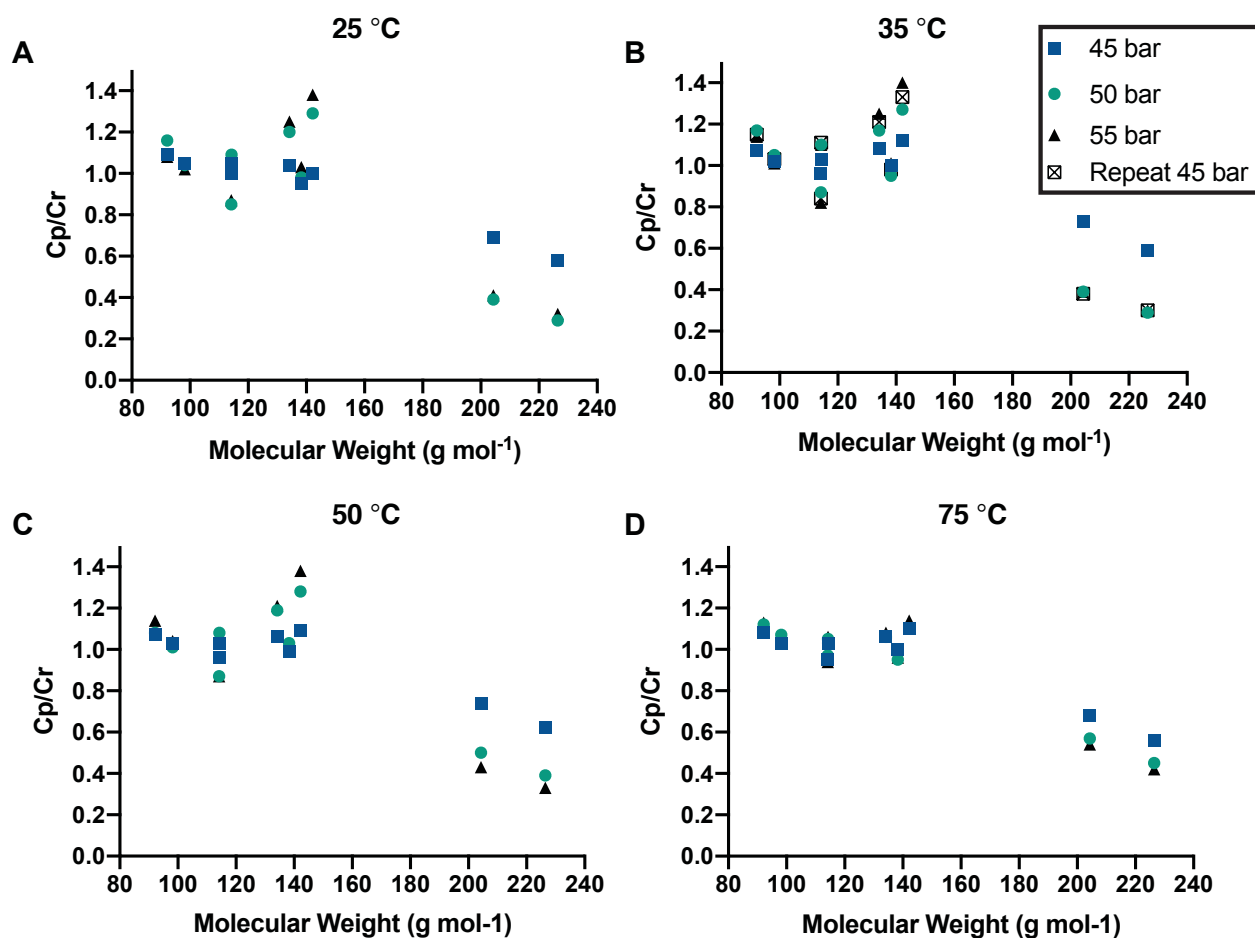
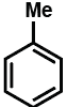
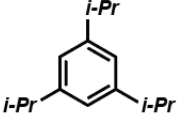
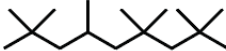
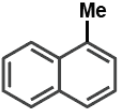
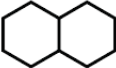


Fig. S25. Ratio of concentrations in permeate vs. retentate (C_p/C_r) of components in the complex mixture outlined in Table S5 for a thin film composite of **SBAD-1** fractionated at various temperatures and pressures. Repeat at 45 bar was completed by recycling the membrane back to 35°C and 45 bar after treatment at 55 bar and showed increased separation performance. The temperature- and pressure-based study spanned a period of 2 months.

Table S6. Some notable separation factors for **SBAD-1** based on data shown in Fig. 3A.

Separation Factors			
	VS.		2.3
$n\text{-C}_8\text{H}_{18}$	VS.		3.2
	VS.		1.4

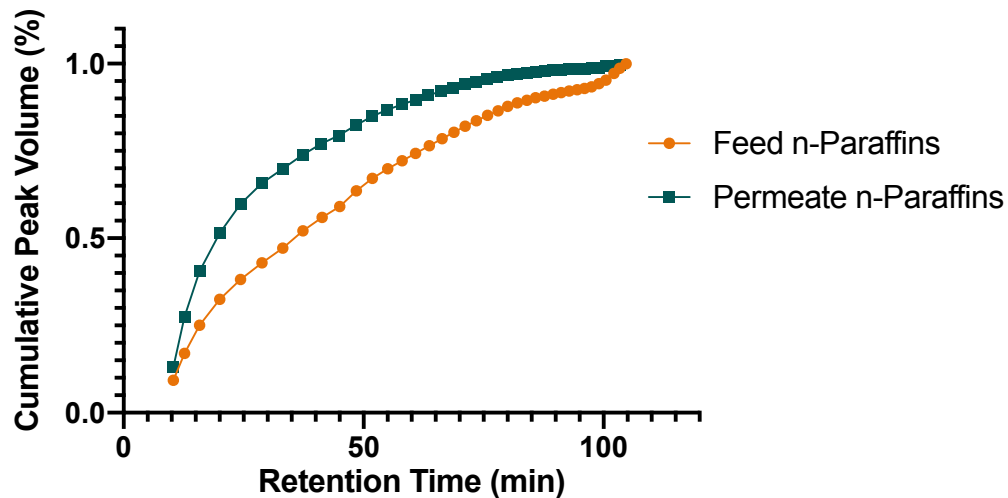


Fig. S26. Comparison of cumulative peak volume curves of the permeate and feed for the **SBAD-1** enrichment of normal paraffin molecules from a whole crude oil separation. Increasing retention time corresponds with increasing molecular weight.

Table S7. Percentage enrichment by hydrocarbon class in the permeate from the crude oil feed for **SBAD-1** at 55 bar and 130 °C. Enrichment was calculated as the area between cumulative peak volume curves of the permeate and feed as shown in Fig. S25.

	Permeance	Class	% Enrichment From Feed
SBAD-1	0.016 (L-m ⁻² -h ⁻¹ -bar ⁻¹)	iso-paraffins	13.5
		aromatics	15.7
		n-paraffins	21.0
		naphthenes	22.5

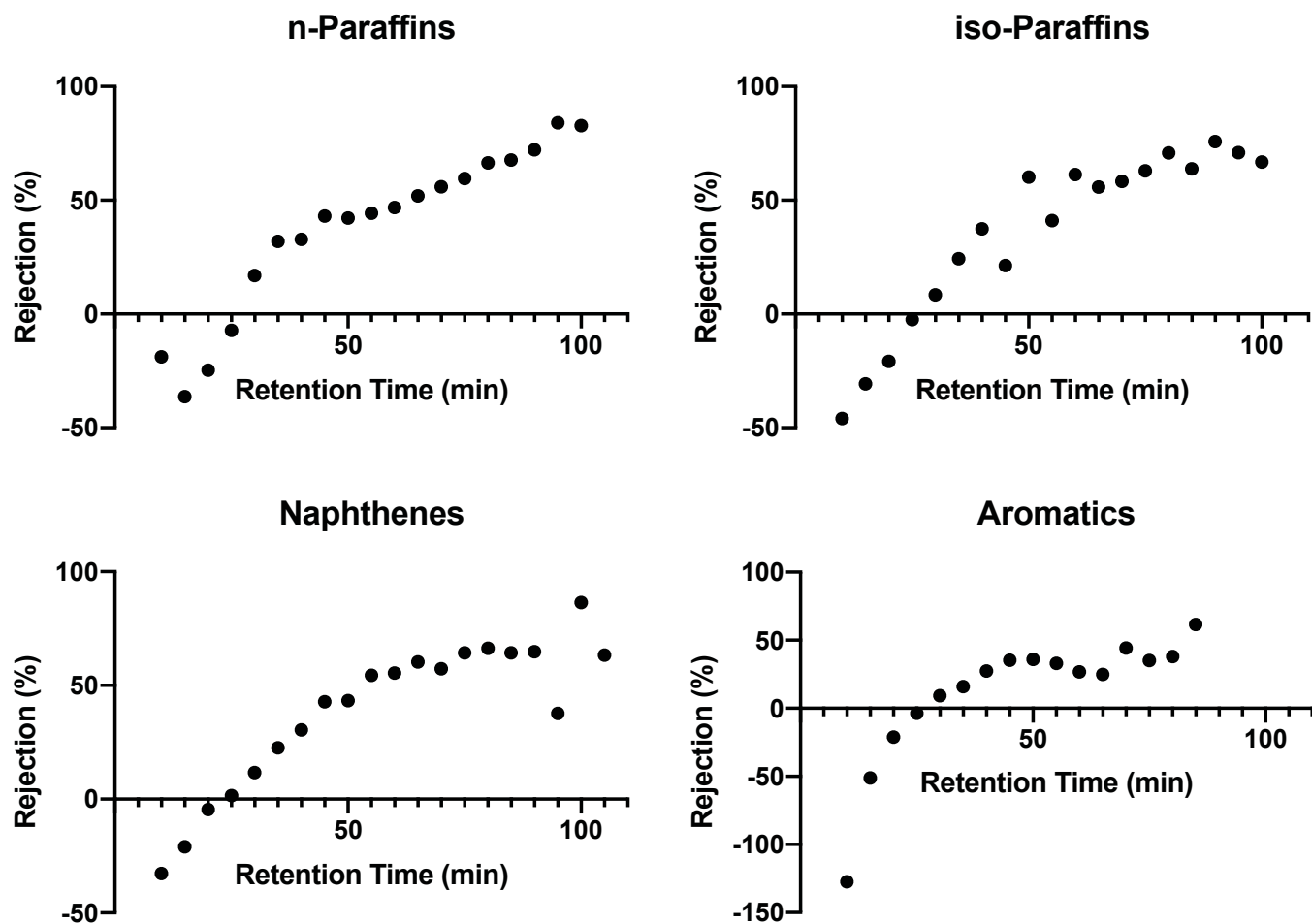


Fig. S27. Rejection curves for individual hydrocarbon classes obtained from GCxGC analysis of crude oil separation by **SBAD-1**. Increasing retention time corresponds to increasing molecular weight within each class.

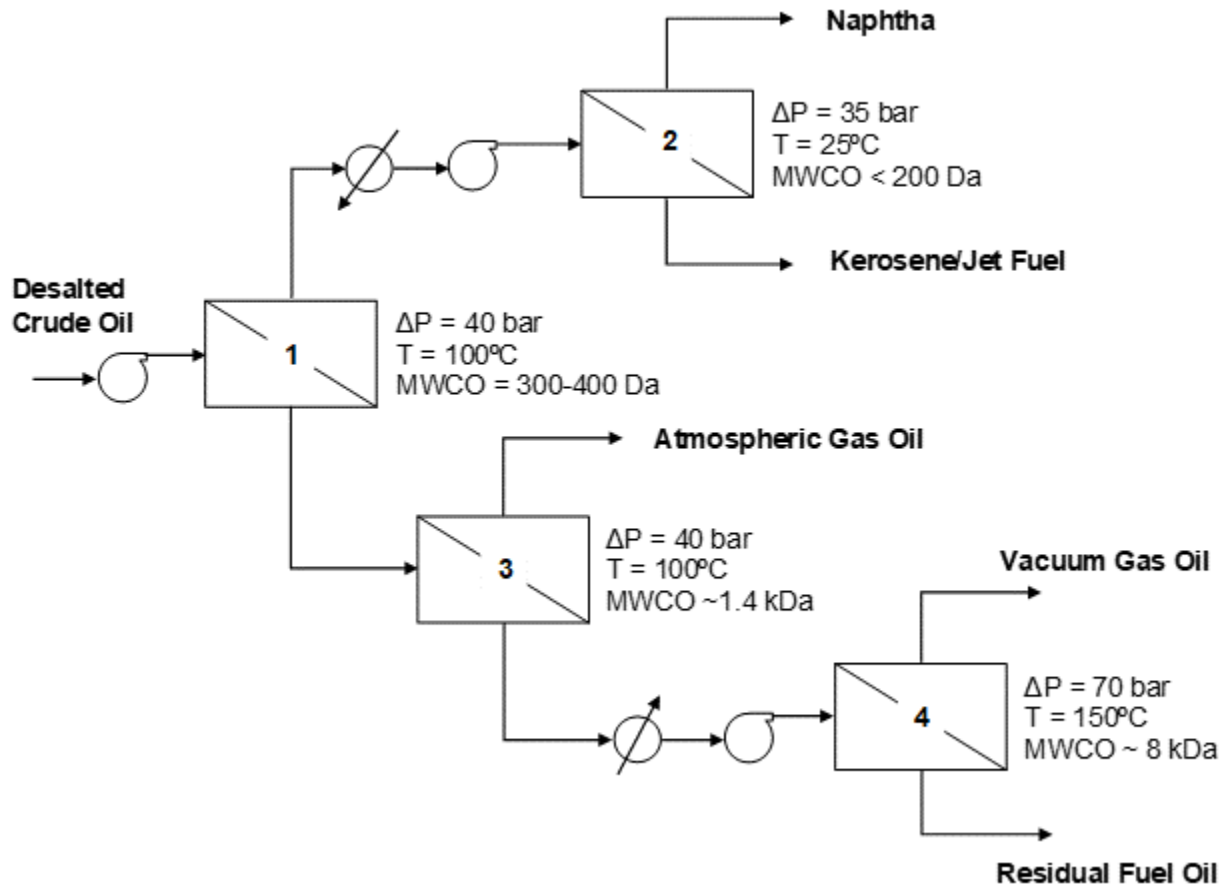
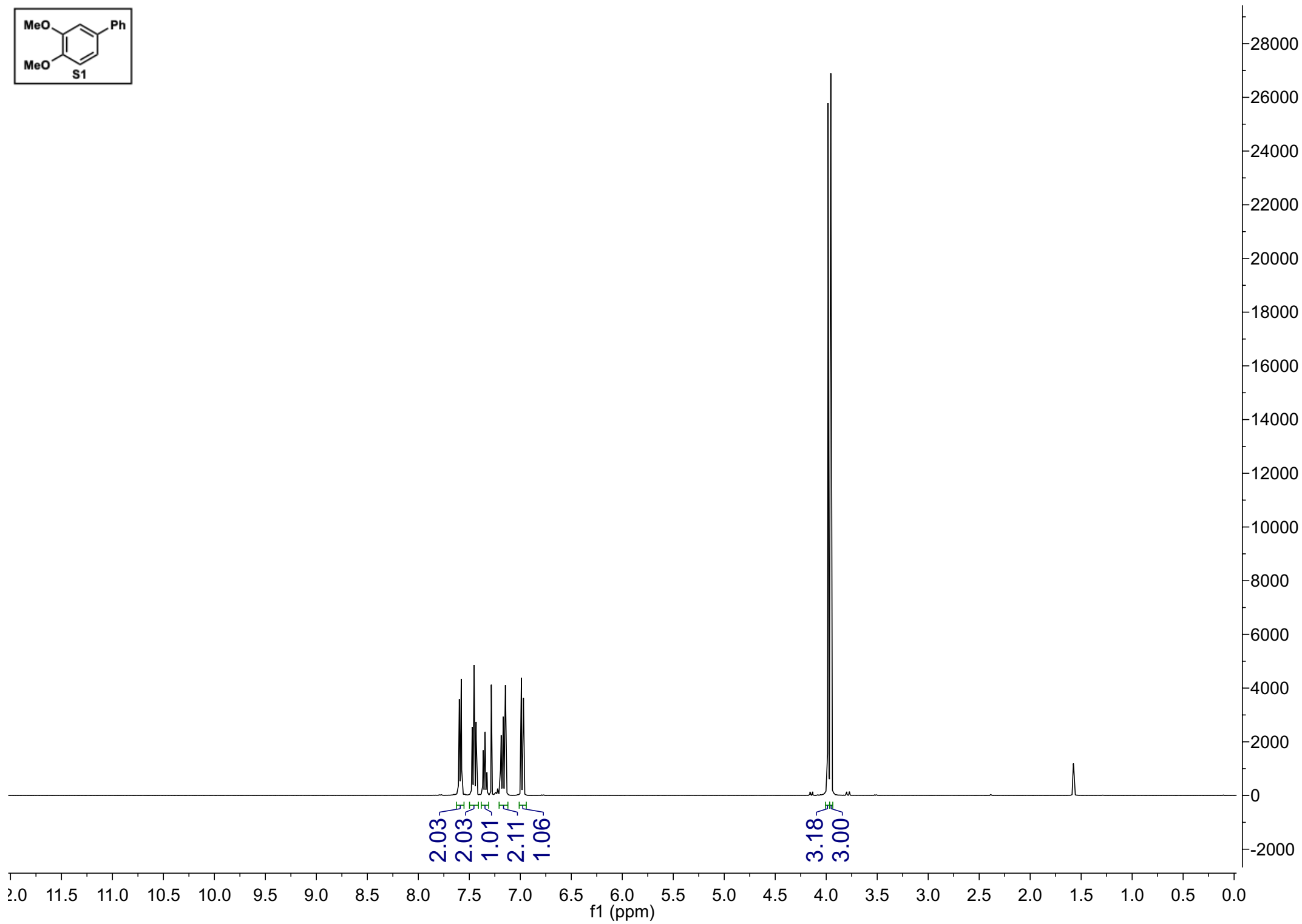
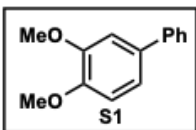
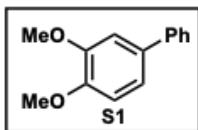


Fig. S28. Exemplary membrane cascade for the separation of crude oil into various fractions (20). Desalted crude oil is fed to membrane stage 1 containing a membrane with molecular weight cut-off (MWCO) in the range of 300-400 Da. Stage 1 permeate is fed to membrane stage 2 with a membrane operating in reverse osmosis or pervaporation mode with MWCO < 200 Da. The permeate and retentate from stage 2 have boiling point distributions in the range of naphtha and kerosene/jet fuel, respectively. Stage 1 retentate is the feed for membrane stage 3, which could consist of a membrane with MWCO ~ 1.4 kDa. The permeate from stage 2 has boiling points mainly in the range of 230-340°C, which corresponds to atmospheric gas oil. Atmospheric gas oil can be further processed into gasoline, diesel and light gas oil. Stage 3 retentate is fed to membrane stage 4, which could consist of an ultrafiltration membrane with MWCO ~ 8 kDa. The permeate from stage 4 has boiling points in the range of 340-570°C, which corresponds to vacuum gas oil. The retentate from this stage can be used in heavy fuel oil/residual fuel oil applications.

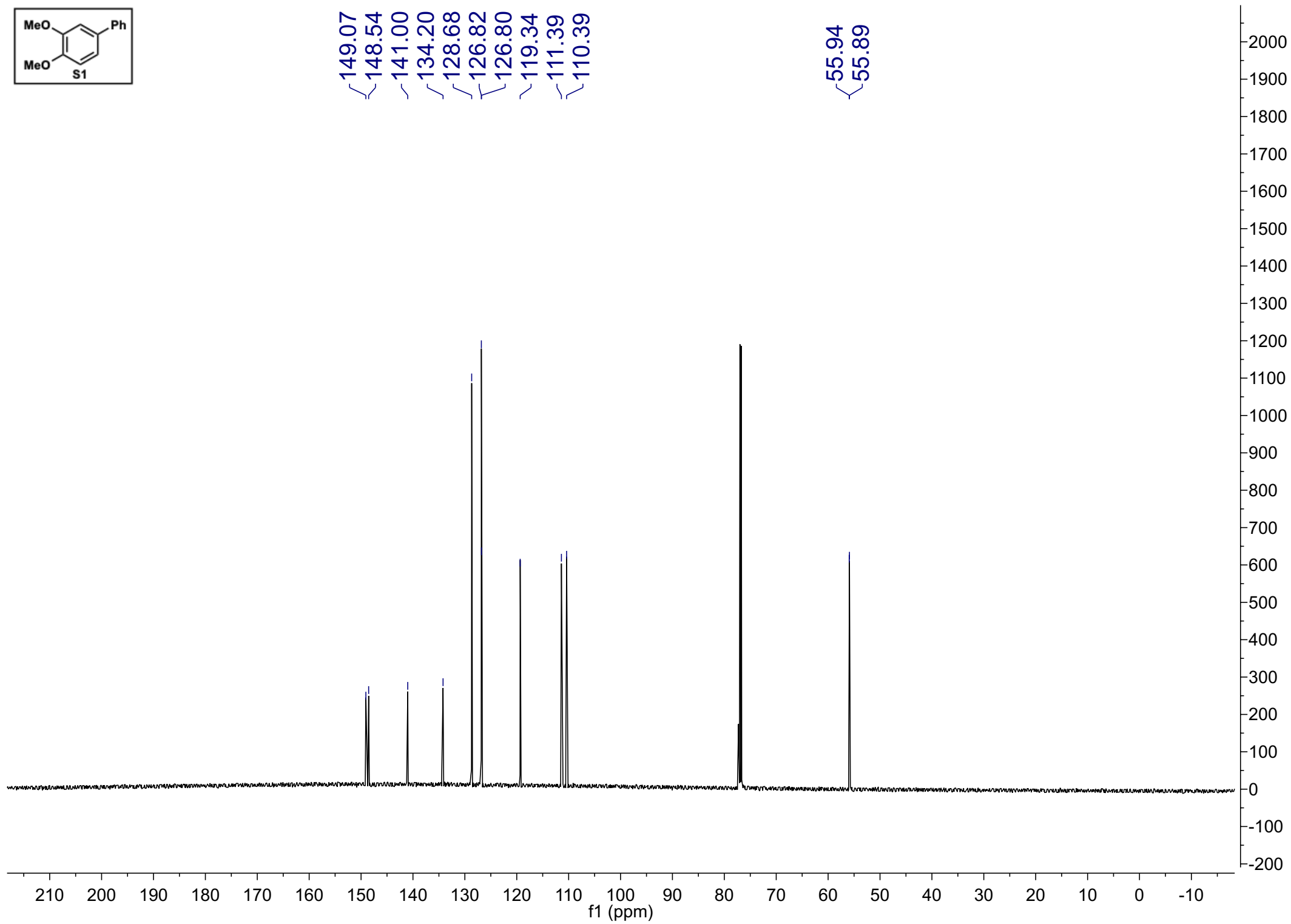
NMR Spectra

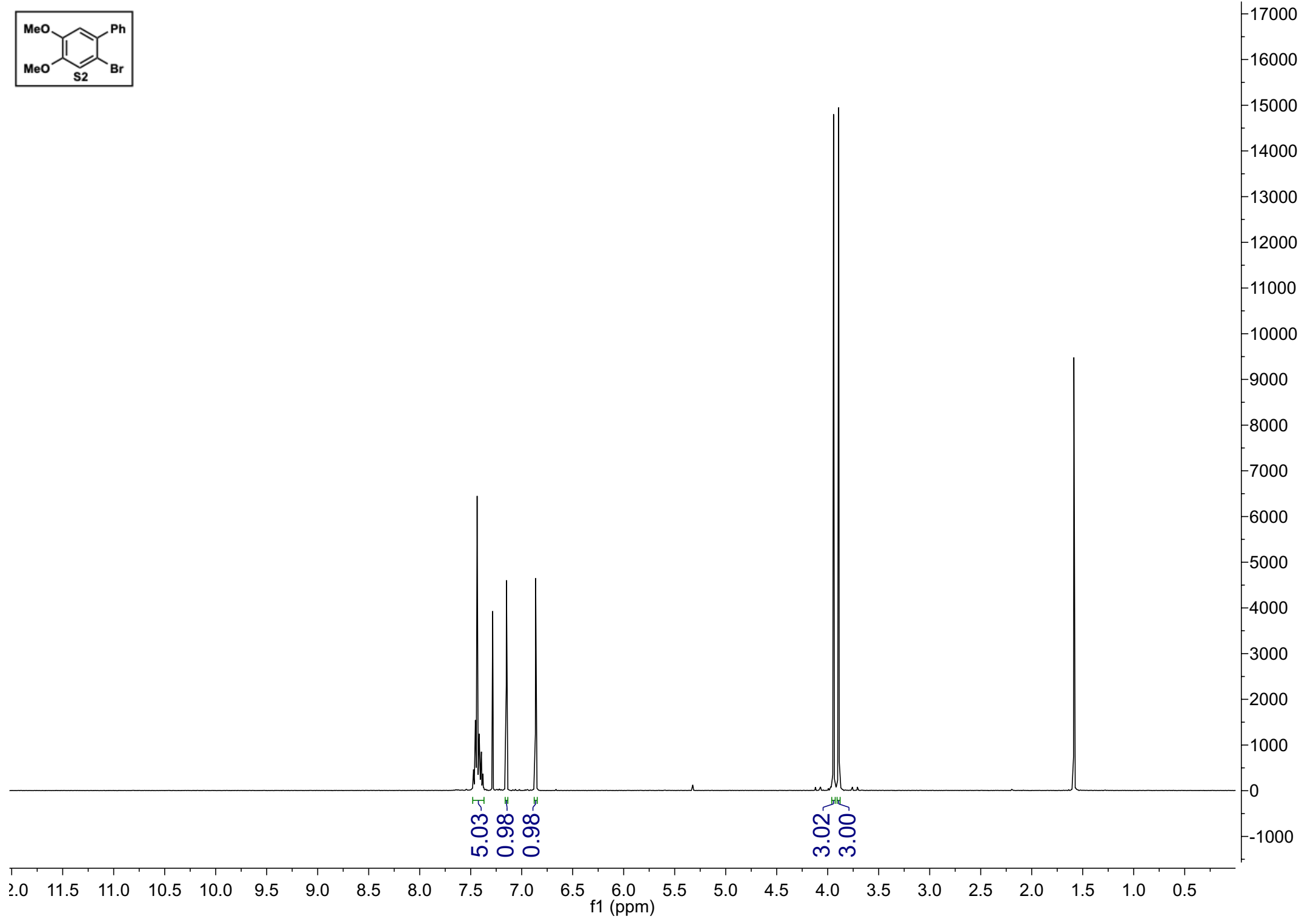
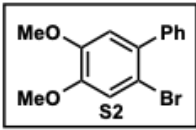


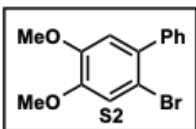


149.07
148.54
141.00
134.20
128.68
126.82
126.80
119.34
111.39
110.39

55.94
55.89

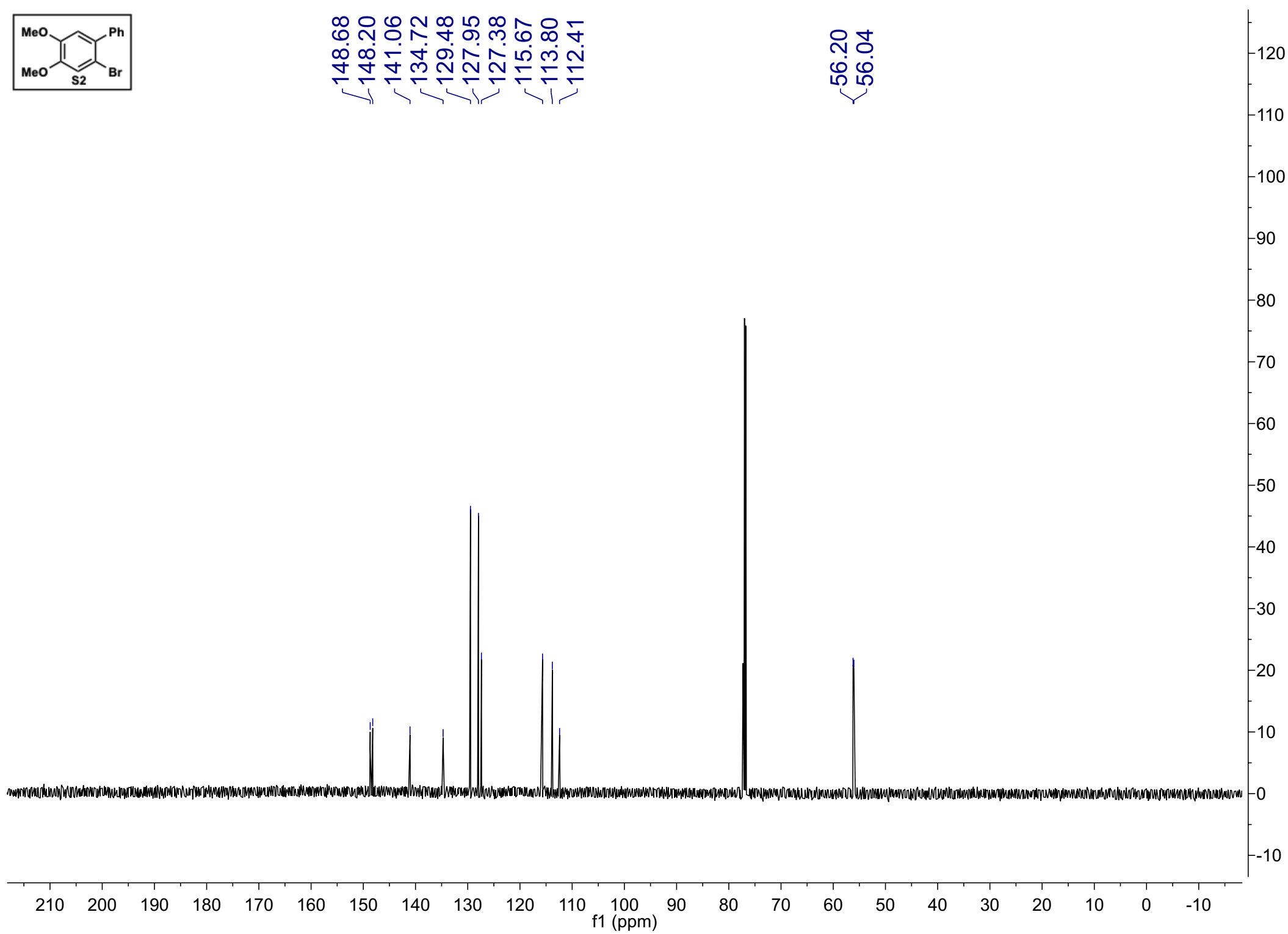


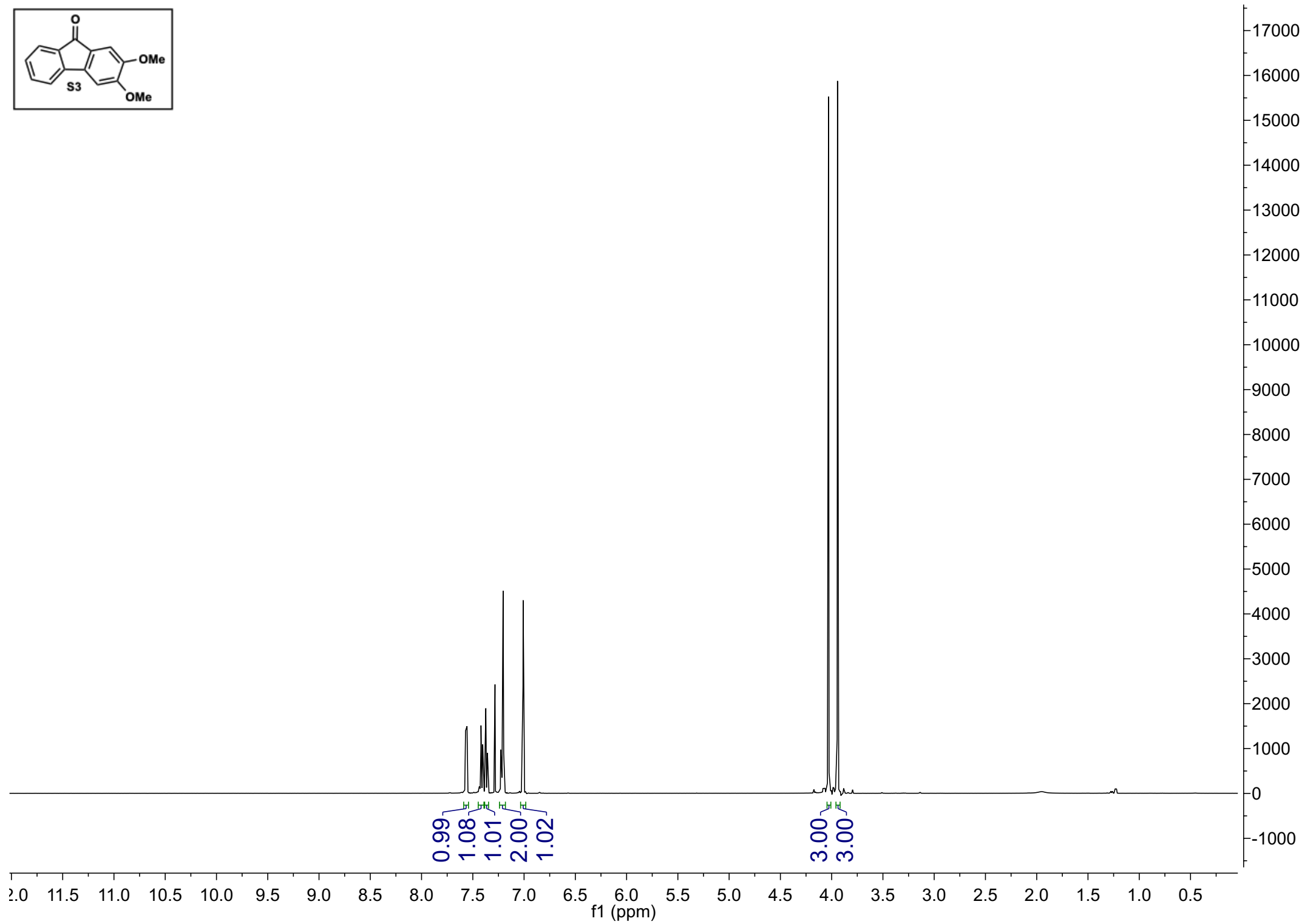
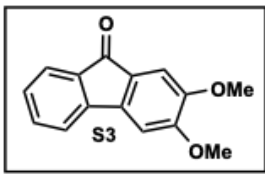


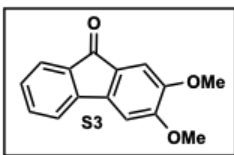


148.68
148.20
141.06
134.72
129.48
127.95
127.38
115.67
113.80
112.41

56.20
56.04



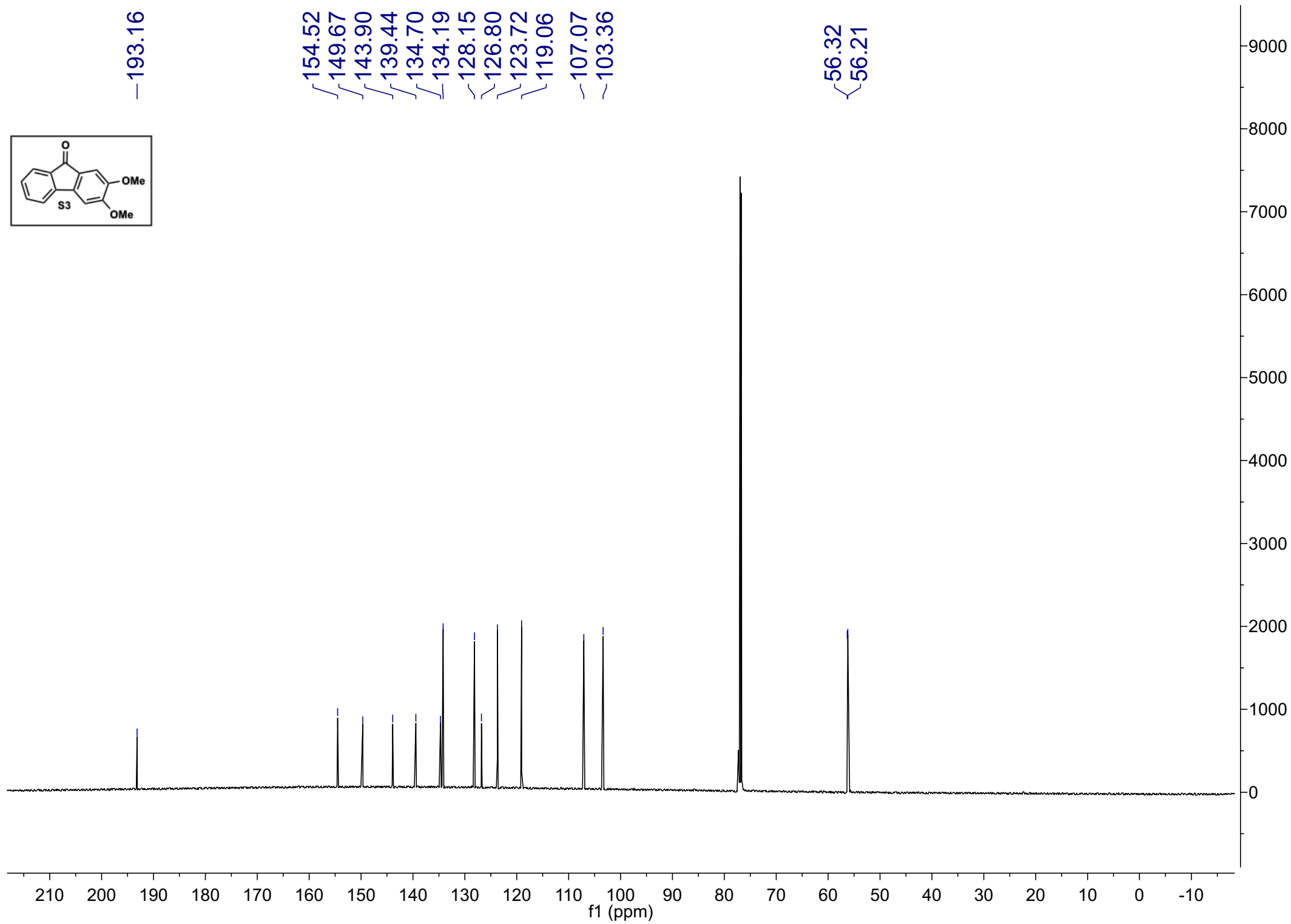


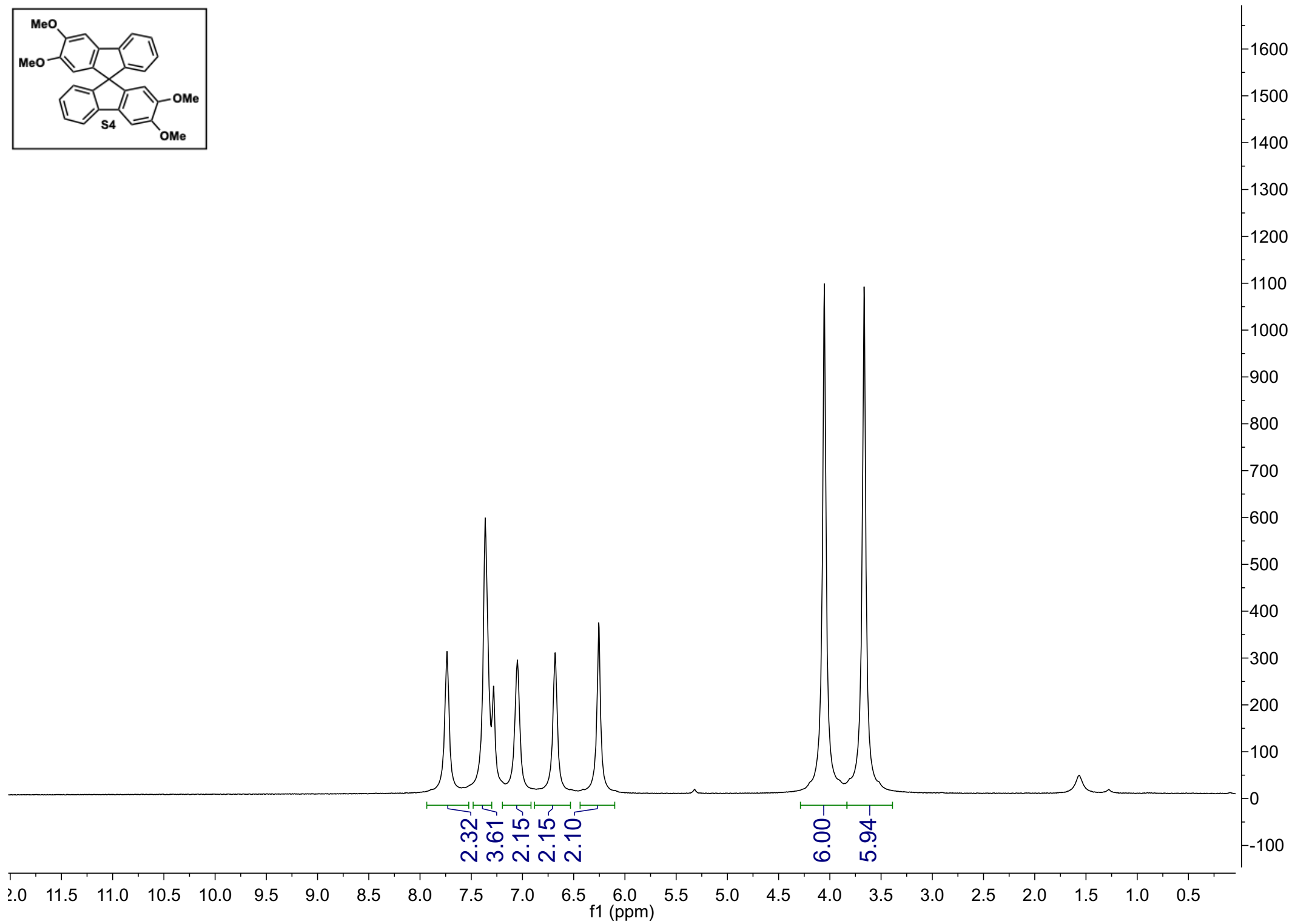
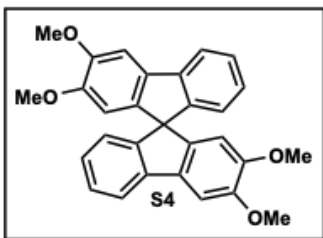


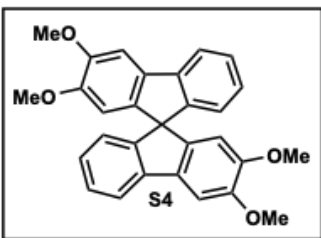
—193.16

154.52
149.67
143.90
139.44
134.70
134.19
128.15
126.80
123.72
119.06
107.07
103.36

56.32
56.21

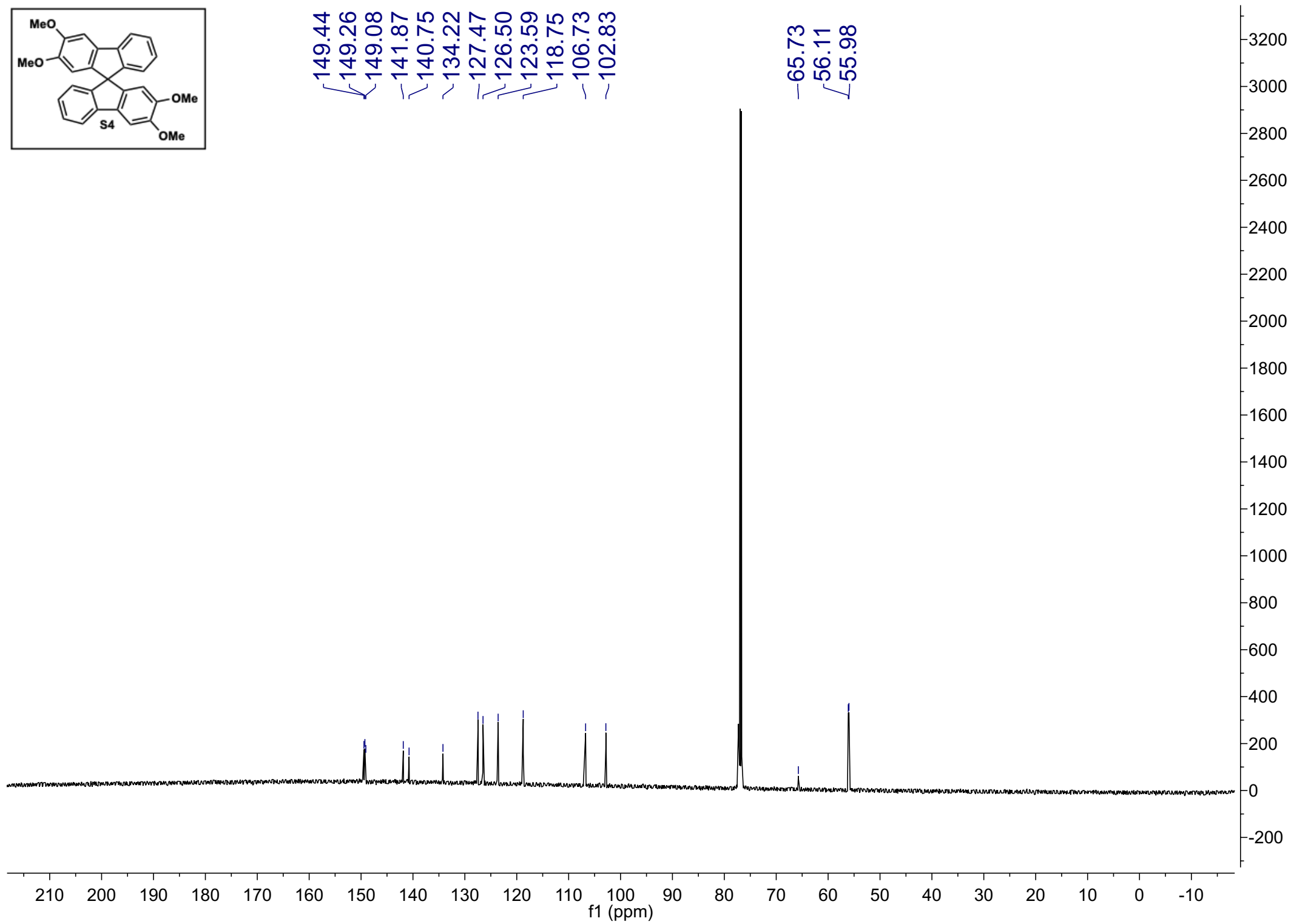


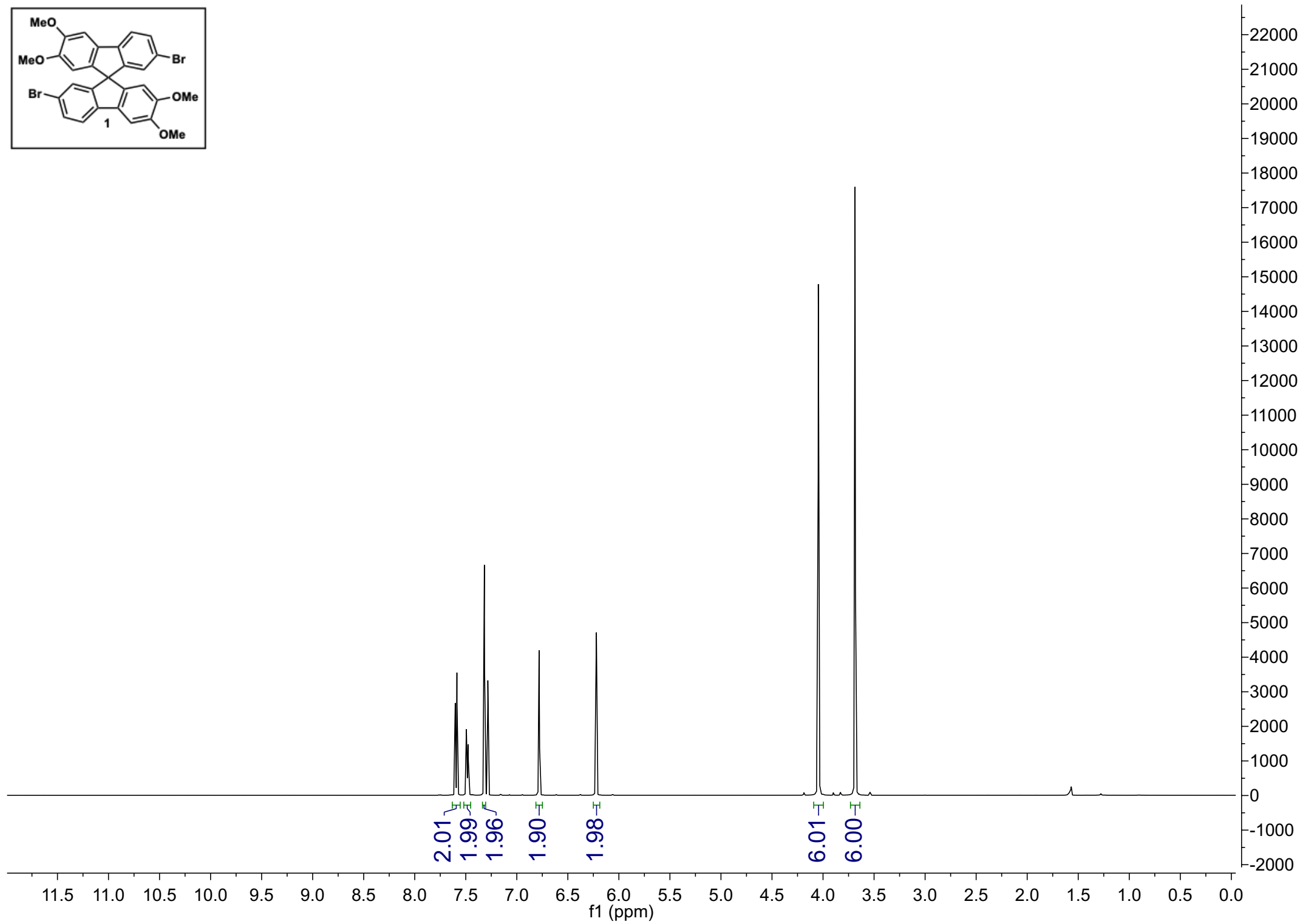
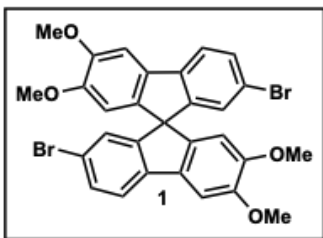


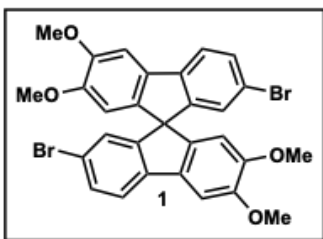


149.44
149.26
149.08
141.87
140.75
134.22
127.47
126.50
123.59
118.75
106.73
102.83

65.73
56.11
55.98

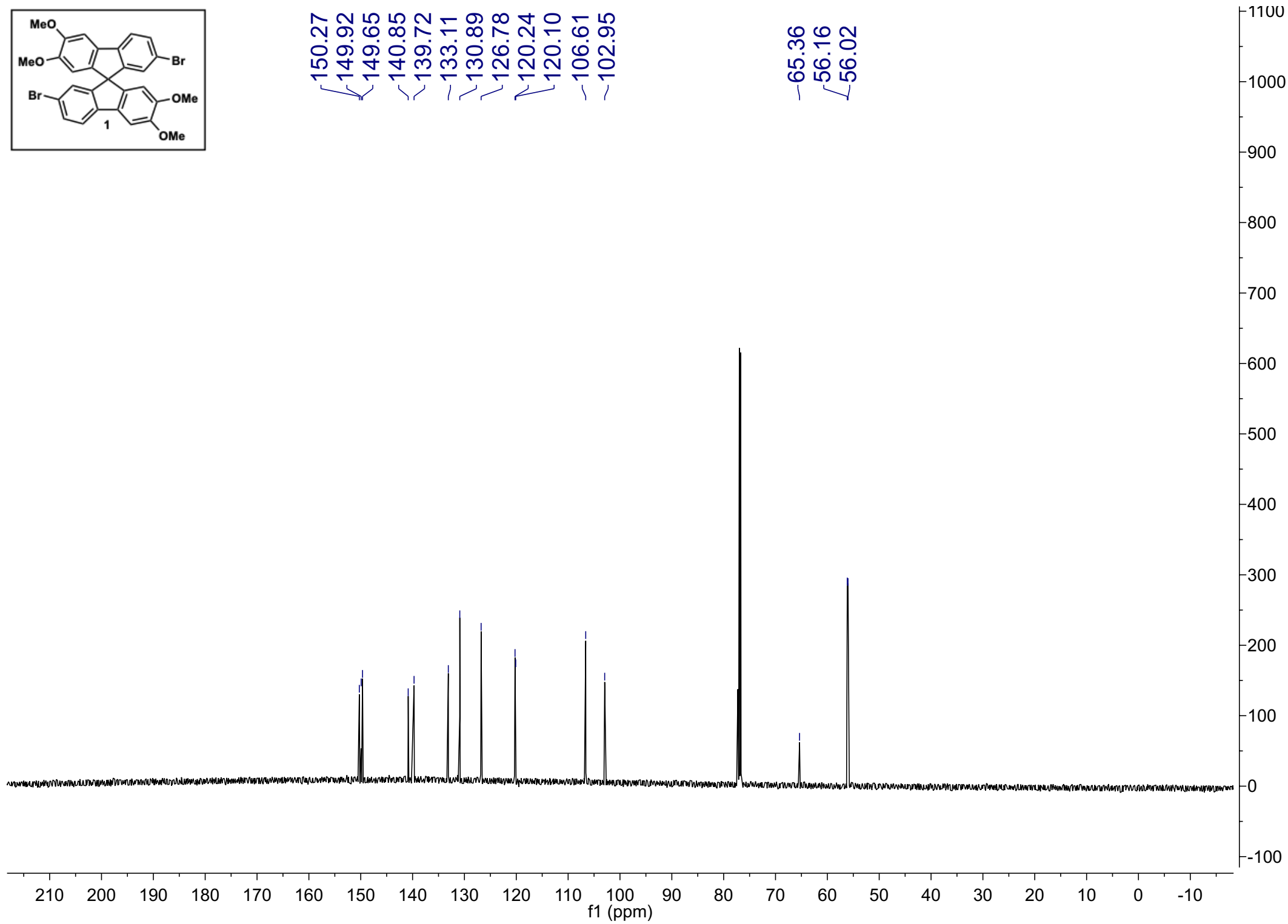


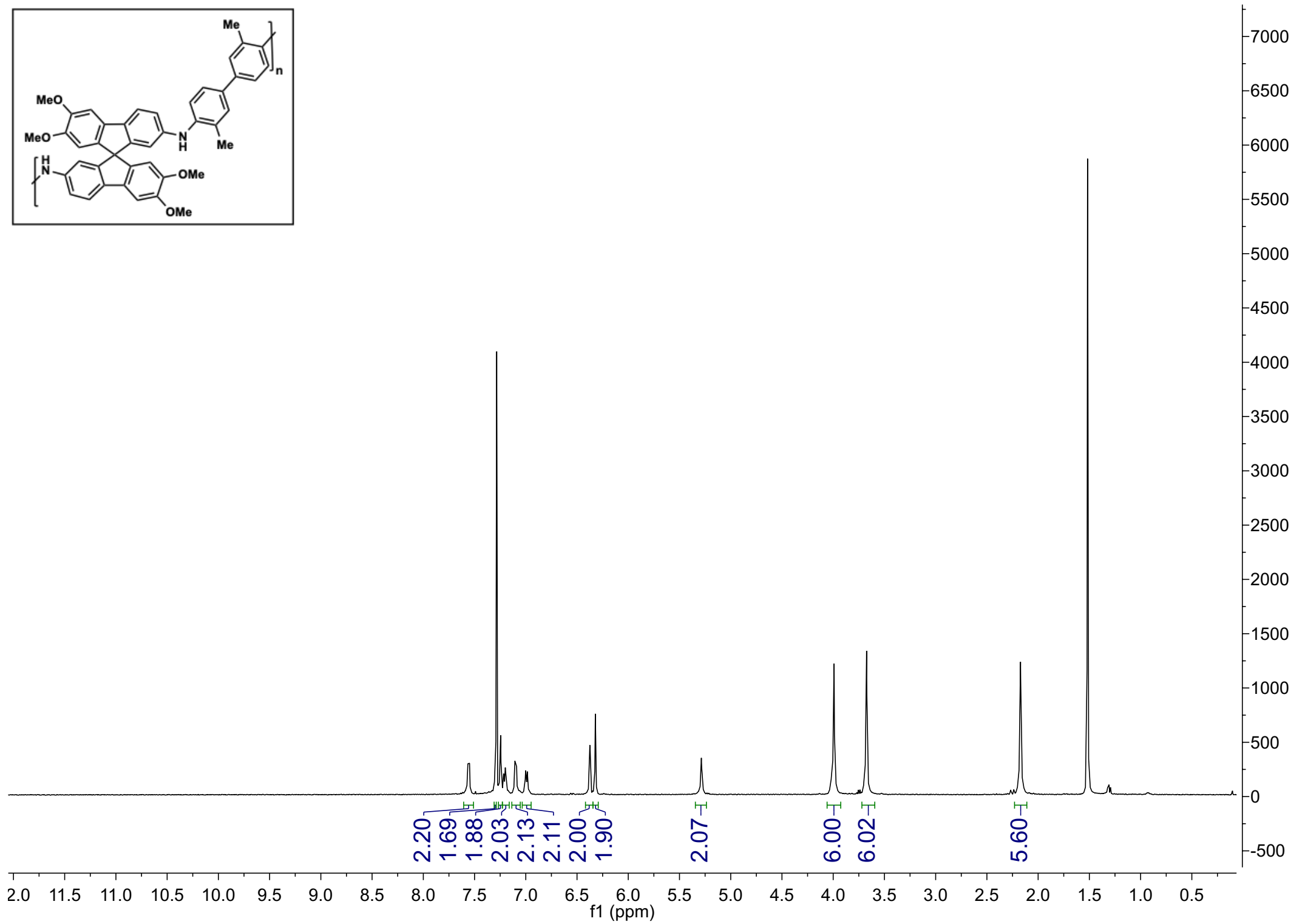
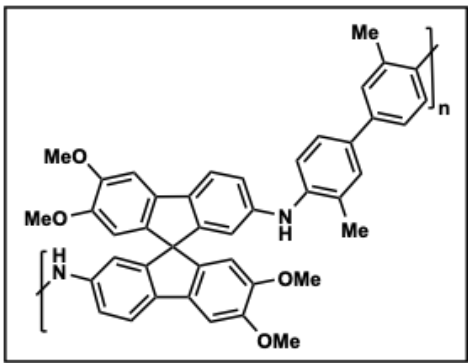


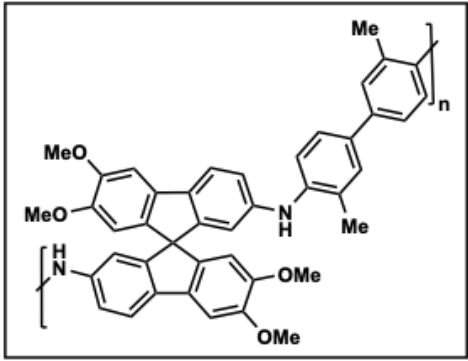


150.27
149.92
149.65
140.85
139.72
133.11
130.89
126.78
120.24
120.10
106.61
102.95

65.36
56.16
56.02



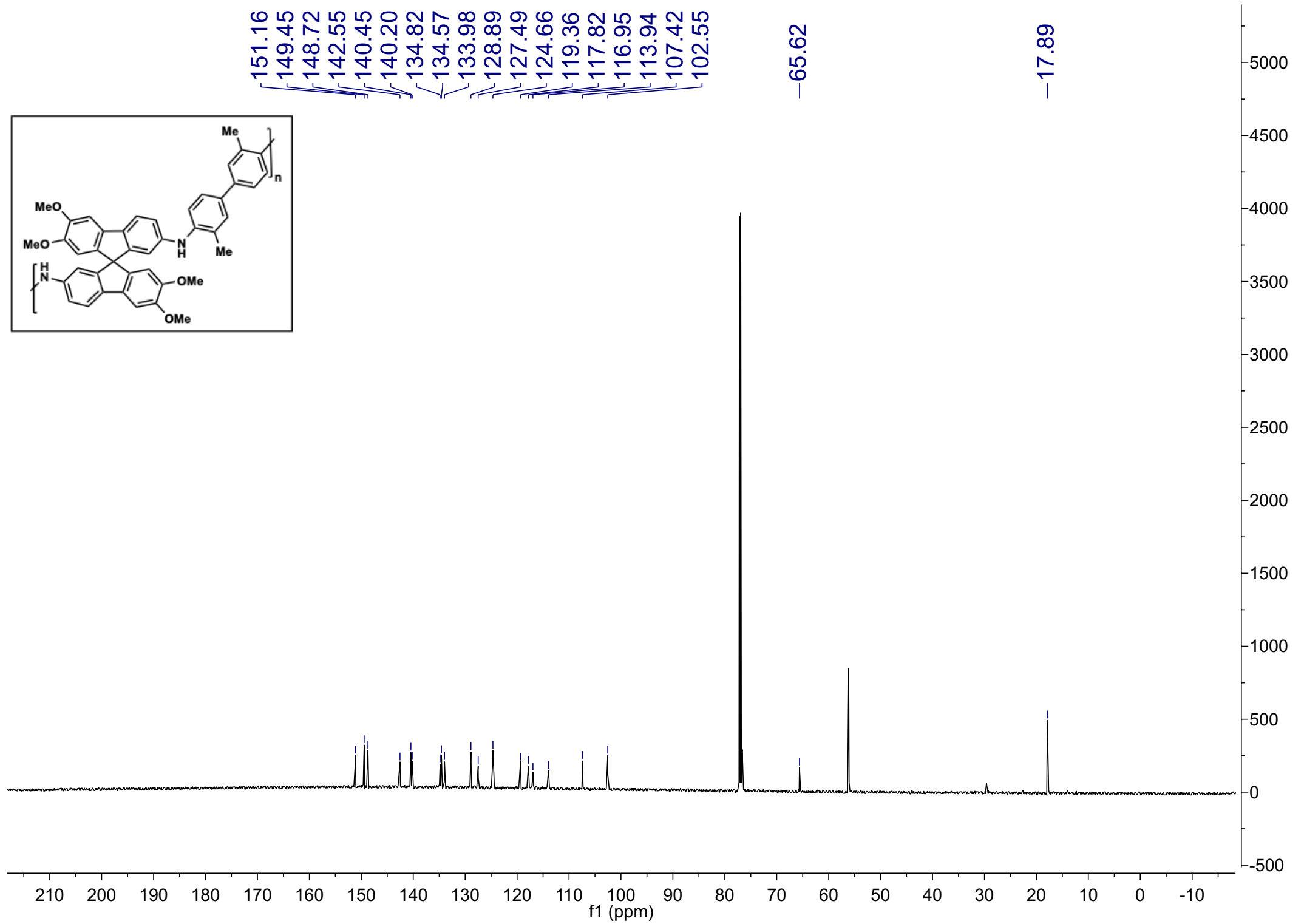


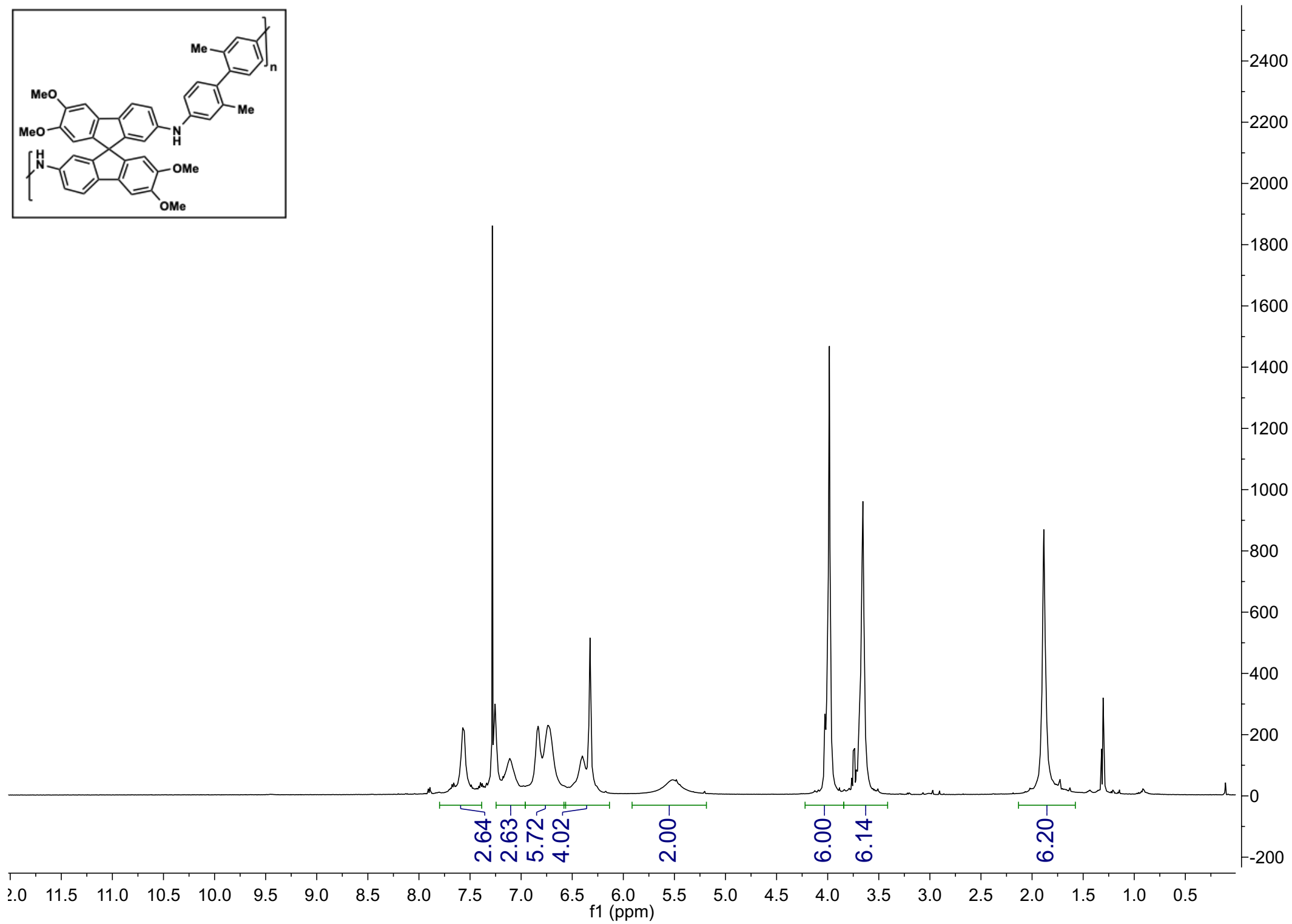
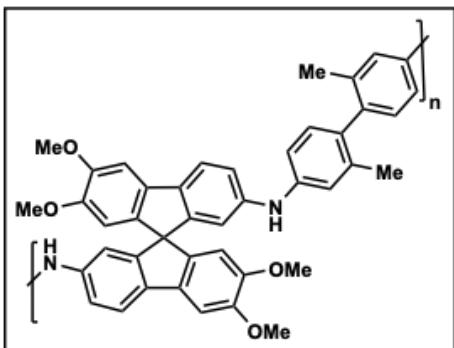


151.16
149.45
148.72
142.55
140.45
140.20
134.82
134.57
133.98
128.89
127.49
124.66
119.36
117.82
116.95
113.94
107.42
102.55

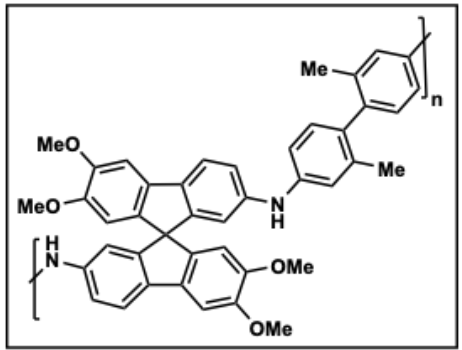
-65.62

-17.89





151.16
149.47
148.79
142.03
141.96
140.42
140.41
137.14
134.97
134.57
133.87
130.53
119.32
118.14
117.08
114.26
107.42
102.63



-65.59
-56.17
-56.10

-19.90

